1988

The effects of transducer cross-axis sensitivity in modal analysis

Sangbo Han
Iowa State University

INFORMATION TO USERS

The most advanced technology has been used to photograph and reproduce this manuscript from the microfilm master. UMI films the text directly from the original or copy submitted. Thus, some thesis and dissertation copies are in typewriter face, while others may be from any type of computer printer.

The quality of this reproduction is dependent upon the quality of the copy submitted. Broken or indistinct print, colored or poor quality illustrations and photographs, print bleedthrough, substandard margins, and improper alignment can adversely affect reproduction.

In the unlikely event that the author did not send UMI a complete manuscript and there are missing pages, these will be noted. Also, if unauthorized copyright material had to be removed, a note will indicate the deletion.

Oversize materials (e.g., maps, drawings, charts) are reproduced by sectioning the original, beginning at the upper left-hand corner and continuing from left to right in equal sections with small overlaps. Each original is also photographed in one exposure and is included in reduced form at the back of the book.

Photographs included in the original manuscript have been reproduced xerographically in this copy. Higher quality 6" x 9" black and white photographic prints are available for any photographs or illustrations appearing in this copy for an additional charge. Contact UMI directly to order.

U·M·I

University Microfilms International
A Bell & Howell Information Company
300 North Zeeb Road, Ann Arbor, MI 48106-1346 USA
313/761-4700 800/521-0600

Order Number 9110504

The effects of transducer cross-axis sensitivity in modal analysis

Han, Sangbo, Ph.D.

Iowa State University, 1988

U·M·I
300 N. Zeeb Rd.
Ann Arbor, MI 48106

The effects of transducer cross-axis sensitivity in modal analysis

by

Sangbo Han

A Dissertation Submitted to the
Graduate Faculty in Partial Fulfillment of the
Requirements for the Degree of
DOCTOR OF PHILOSOPHY

Department: Engineering Science and Mechanics
Major: Engineering Mechanics

Approved:

Signature was redacted for privacy.

In Charge of Major Work

Signature was redacted for privacy.

For the Major Department

Signature was redacted for privacy.

For the Graduate College

Iowa State University
Ames, Iowa
1988

TABLE OF CONTENTS

		Page
I.	INTRODUCTION	1
II.	THEORETICAL DEVELOPMENT	5
III.	EXPERIMENTAL PROCEDURES	12
A.	Accelerometer Calibration in Time Domain	12
B.	Accelerometer Calibration in Frequency Domain	16
C.	Impact Hammer Calibration	18
D.	Vibration Measurement	19
1.	Experimental apparatus	19
2.	Frequency analyzer description	21
3.	Baseband measurement	23
4.	Zoom measurement	24
IV.	RESULTS AND DISCUSSION	26
A.	Frequency Response Functions with Baseband Measurement	26
B.	Frequency Response Functions with Zoom Measurement	29
C.	Modal Parameters Extracted	31
D.	Mode Shapes	35
V.	CONCLUSIONS AND RECOMMENDATIONS	38
VI.	BIBLIOGRAPHY	41
VII.	ACKNOWLEDGMENTS	44
VIII.	TABLES AND FIGURES	45
IX.	APPENDIX A. BRIEF REVIEW OF THEORETICAL ASPECTS OF MODAL ANALYSIS	82

A. General 82

B. Modal Parameter Extraction Methods 84

1. Search peak method 85

2. Circle fit method 86

3. Complex exponential method 88

X. APPENDIX B. TRANSVERSE SENSITIVITY OF PIEZOELECTRIC ACCELEROMETER 95

I. INTRODUCTION

Major advances in computers, digital analyzers and numerical algorithms have made experimental modal analysis a vital part of the study of structural vibrations. The objective of modal analysis is to extract characteristic parameters of a structure such as natural frequencies, damping values, and mode shapes from experimentally obtained structural responses. Therefore, a successful experimental modal analysis requires accurate and reliable measurement of a structures vibration response.

An accelerometer is a transducer that is commonly used to measure vibration response of a structure. It is well known that these transducers have an unwanted cross-axis sensitivity; that is, they are sensitive to accelerations in a direction perpendicular to the primary sensing axis of the transducer. Usually, this cross-axis sensitivity is less than 10 percent of the primary sensing axis sensitivity. This cross-axis sensitivity can be neglected if the primary sensing axis is accurately aligned with the direction of structural motion. However, it is particularly difficult to align the primary sensing axis and the direction of structural motion when testing an unknown structure.

Consider a typical procedure for testing the three dimensional vibration behavior of a structure. Unidirectional or triaxial transducers are attached to the structure at various locations and are oriented in various defined directions in order to measure the structural response to a given excitation. It is common practice to

interpret the output of each transducer as the structural motion in the direction of the primary sensing axis. This is common practice regardless of either the amount of cross-axis sensitivity or the amount of structural motion in the direction perpendicular to the primary sensing axis of the transducer. Thus, under certain resonance conditions, it is possible that the response of the structure is in a direction that is nearly perpendicular to the primary sensing axis of the transducer and results in the output signal being dominated by the cross-axis motion. In addition, if there is a coupled mode with other directions [1], either translational or rotational, the potential errors are enormous.

Figure 1 (located at the back of this dissertation starting at page 49) shows an example of above mentioned misalignment between the direction of primary sensing axis and that of response for a general structure which undergoes both translational and rotational motion. The position and direction of the attached accelerometer shows an intent to measure only the translational motion, in the direction of PP'. This direction is parallel to the accelerometer's primary sensing axis, while the actual response picked by the accelerometer is the combined motion of translation and rotation, along path PP". In this particular case, the actual response (PP") can be decomposed into translational motion (PP') and rotational motion (P'P"). The normal component of rotational motion (P'P") will be merged into primary sensing axis signal while the tangential component will be sensed by the accelerometer's cross-axis sensitivity. When the natural frequencies of these two modes

(translational and rotational) are close together, an underestimated or overestimated frequency response function is created. However, if the two natural frequencies are well separated compared to the frequency resolution of the measurement system, the combined effect of cross-axis sensitivity and coupled modes creates additional peaks in the measured frequency response function.

There are several methods available to separate and identify these peaks both during the measurement stage [2][3] and during the data analysis stage [4]. However, the fundamental assumption that is made in the application of any of these methods is: "all of the peaks that appear in the frequency response function are due to natural modes of vibration with motion in the direction of the primary sensing axis of the transducer." Furthermore, sophisticated algorithms may lead to confusing results as illustrated in Fig. 2 [5][6]. In Fig. 2(a), only two natural modes are identified from the frequency response function where additional peaks are obviously neglected during data analysis stage. On the other hand, in Fig. 2(b) ten different natural modes are identified from this frequency response function where separated peaks are barely recognizable.

The objective of experimental modal analysis is to define the dynamic characteristics of a structure in terms of its modal parameters. These parameters are defined by the natural frequencies, the mode shapes, and the modal dampings. The successful calculation of these modal parameters is highly dependent on the quality of the frequency response function. The purpose of this research is to show how the

parasitic peaks in the frequency response function that are due to the cross-axis sensitivity of the transducer can be eliminated at an early stage before proceeding with the calculation of the modal parammeters. The implied erroneous signal due to cross-axis sensitivity can be compensated for in either the time domain or the frequency domain of the signal depending on which compensation is convenient and appropriate for the data acquisition and signal processing system employed. Experimental frequency response functions from a uniform rectangular beam are used to demonstrate the effects of this compensation.

II. THEORETICAL DEVELOPMENT

The construction used in the design of a transducer significantly effects its cross-axis sensitivity characteristics. For the purpose of this section, Fig. 3 graphically shows the sensitivity characteristics of a single transducer.

The primary sensing axis is labled 1 and its corresponding voltage sensitivity is called S_{11}; i.e., volts/unit measured(m/s^2, g's). The cross-axis sensitivity plane is perpendicular to the primary sensing axis as shown. The ideal cross-axis sensitivity $S_{1\theta}$ is the output voltage/unit of input motion in direction θ where direction θ lies in the cross-axis plane as shown. Ideally $S_{1\theta}$ is zero. The next best ideal is for $S_{1\theta}$ to be a constant. Physically, it is shown in Appendix B that $S_{1\theta}$ can not be a constant independent of angle θ as shown by the constant radius. Unfortunately, $S_{1\theta}$ is a function of angle θ. This means that the values of cross-axis sensitivity are dependent on the directions selected for axis 2 and 3. When a given transducer is mounted on a triaxial mounting block, the cross-axis sensitivities must be determined for the condition as mounted to the block.

For the purpose of dealing with a triaxial accelerometer, the mounting block is assumed to have three mutually perpendicular axes labeled x, y, and z. Then each accelerometer has three voltage sensitivities S_{ix}, S_{iy} and S_{iz} where the subscript i is dependent on whether the primary sensing axis corresponds to the x, y, or z

directions. The values of the cross-axis sensitivities depend on the orientation of the other two orthogonal directions in the cross-axis plane. In all, nine sensitivities are required to describe the input acceleration and output voltage relationships for a triaxial accelerometer. These relationships are:

$$\begin{bmatrix} S_{xx} & S_{xy} & S_{xz} \\ S_{yx} & S_{yy} & S_{yz} \\ S_{zx} & S_{zy} & S_{zz} \end{bmatrix} \begin{Bmatrix} a_x \\ a_y \\ a_z \end{Bmatrix} = \begin{Bmatrix} E_x \\ E_y \\ E_z \end{Bmatrix} \qquad (1)$$

where S_{ij} - voltage sensitivity in the i direction due to acceleration in j direction

a_j - input acceleration in j direction

E_i - output voltage from transducer mounted with primary sensitivity axis in i direction.

It is important to remember that the cross-axis sensitivities <u>are not necessarily the maximum</u> cross-axis sensitivities of the transducer, and that the sensitivity terms can be either positive or negative depending on how the transducers are mounted and directions assumed to be positive.

The input accelerations a_j can be solved for from Eq. (1). Since the maximum cross-axis sensitivities are usually less than 5 percent of the primary axis sensitivity, the accelerations can be approximated by

$$a_x = \left(\frac{E_x}{S_{xx}}\right) - \left(\frac{S_{xy}}{S_{xx}}\right)\left(\frac{E_y}{S_{yy}}\right) - \left(\frac{S_{xz}}{S_{xx}}\right)\left(\frac{E_z}{S_{zz}}\right)$$

$$a_y = -\left(\frac{S_{yx}}{S_{yy}}\right)\left(\frac{E_x}{S_{xx}}\right) + \left(\frac{E_y}{S_{yy}}\right) - \left(\frac{S_{yz}}{S_{yy}}\right)\left(\frac{E_z}{S_{zz}}\right) \qquad (2)$$

$$a_z = -\left(\frac{S_{zx}}{S_{zz}}\right)\left(\frac{E_x}{S_{xx}}\right) - \left(\frac{S_{zy}}{S_{zz}}\right)\left(\frac{E_y}{S_{yy}}\right) + \left(\frac{E_z}{S_{zz}}\right)$$

which can be rewritten as

$$\begin{aligned} a_x &= a_{xo} - \varepsilon_{xy}\, a_{yo} - \varepsilon_{xz}\, a_{zo} \\ a_y &= -\varepsilon_{yx}\, a_{xo} + a_{yo} - \varepsilon_{yz}\, a_{zo} \\ a_z &= -\varepsilon_{zx}\, a_{xo} - \varepsilon_{zy}\, a_{yo} + a_{zo} \end{aligned} \qquad (3)$$

where

$$\begin{aligned} a_{xo} &= E_x / S_{xx} \\ a_{yo} &= E_y / S_{yy} \\ a_{zo} &= E_z / S_{zz} \end{aligned} \qquad (4)$$

are the commonly used but contaminated acceleration time history signals. These signals are usually considered to be the true acceleration time histories. The normalized transducer sensitivity ε_{ij} is related to the corresponding voltage sensitivities by

$$\varepsilon_{ij} = S_{ij} / S_{ii} \qquad (5)$$

from which it is apparent that $\varepsilon_{ii}=1.0$. Thus, Eq. (3) can be written as

$$\begin{Bmatrix} a_x \\ a_y \\ a_z \end{Bmatrix} = \begin{bmatrix} \varepsilon_{xx} & -\varepsilon_{xy} & -\varepsilon_{xz} \\ -\varepsilon_{yx} & \varepsilon_{yy} & -\varepsilon_{yz} \\ -\varepsilon_{zx} & -\varepsilon_{zy} & \varepsilon_{zz} \end{bmatrix} \begin{Bmatrix} a_{xo} \\ a_{yo} \\ a_{xo} \end{Bmatrix} = [\ \varepsilon\ ]\ \{\ a_o\ \} \qquad (6)$$

The ε matrix in Eq. (6) gives a quick overall view of the potential cross-axis contamination of the triaxial accelerometer signals.

The amount of approximation used in Eq. (6) can be illustrated by comparing the expression for a_x with that obtained from using Cramer's rule on Eq. (1). The complete expression is

$$a_x = \frac{(1-\varepsilon_{zy}\varepsilon_{yz})}{(1-\varepsilon^*)} a_{xo} - \frac{(\varepsilon_{xy}-\varepsilon_{xz}\varepsilon_{zy})}{(1-\varepsilon^*)} a_{yo} - \frac{(\varepsilon_{xz}-\varepsilon_{xy}\varepsilon_{yz})}{(1-\varepsilon^*)} a_{zo} \qquad (7)$$

where the denominator $(1-\varepsilon^*)$ comes from the determinant of the sensitivity matrix. The denominator error term ε^* is given by

$$\varepsilon^* = \varepsilon_{yz}\varepsilon_{zy} + \varepsilon_{xz}\varepsilon_{zx} + \varepsilon_{xy}\varepsilon_{yx} - \varepsilon_{xy}\varepsilon_{yz}\varepsilon_{zx} - \varepsilon_{xz}\varepsilon_{yx}\varepsilon_{zy} \qquad (8)$$

If each cross-axis sensitivity term $\varepsilon_{ij} = 0.10$, the coefficient on a_{xo} becomes 1.02 or the linearized term is off by 2%. The coefficient on a_{yo} and a_{zo} will be in error by 8%. But if $\varepsilon_{ij} = 0.05$ for each term, the error become 0.5% on a_{xo} and 4.5% on the a_{yo} and a_{zo} terms. Thus, Eq. (6) is sufficiently accurate for the purpose of correcting the apparent accelerations, a_{xo}, a_{yo}, and a_{zo}, since the order of the ε_{ii} is

that of essentially unity while that of ε_{ij} is of the order of 0.05 or less.

Equation (6) can be used to correct the original time histories in the time domain before the frequency analysis is performed on the signals. The major problem with this technique is that every time history must be processed before the frequency analysis is performed and then averaged. It would be simpler if the correction could be done on the averaged FRFs in order to reduce the required number of computations.

The Fourier transform of the finite time histories in Eq. (1) can be processed using the same small ε_{ij} approximations to give

$$\begin{Bmatrix} A_x \\ A_y \\ A_z \end{Bmatrix} = \begin{bmatrix} & \varepsilon & \end{bmatrix} \begin{Bmatrix} A_{xo} \\ A_{yo} \\ A_{zo} \end{Bmatrix} \tag{9}$$

where A_i = $A_i(\omega)$ is the Fourier transform of the true acceleration in the ith direction and

A_{io} = $A_{io}(\omega)$ is the Fourier transform of the signal from transducer.

i = x, y, and z.

Now, starting with Eq. (9) and neglecting second order terms, the power spectral densities of the true structural accelerations are given by

$$
\begin{aligned}
G_{xx} &= G_{xoxo} - \varepsilon_{xy}(G_{yoxo} + G_{xoyo}) - \varepsilon_{xz}(G_{zoxo} + G_{xozo}) \\
G_{yy} &= G_{yoyo} - \varepsilon_{yx}(G_{xoyo} + G_{yoxo}) - \varepsilon_{yz}(G_{zoyo} + G_{yozo}) \\
G_{zz} &= G_{zozo} - \varepsilon_{zx}(G_{xozo} + G_{zoxo}) - \varepsilon_{zy}(G_{yozo} + G_{zoyo})
\end{aligned} \tag{10}
$$

where G_{ioio} represent the measured signal power spectral densities

G_{iojo} represent the measured signal cross spectral densities

G_{ii} represent the actual power spectral densities of the structural motion.

Equation (10) shows that the power spectrum of the output motion is not equal to the power spectrum of the signal; i.e., $G_{xx} = G_{xoxo}$. The cross spectral densities are seen as the correction terms along with the normalized cross-axis sensitivities.

However, for the purpose of experimental modal analysis, it is desired to obtain the corrected frequency response functions (FRFs). These corrections can be obtained by forming the cross spectral density of each term in Eq. (9) with the spectral density of the excitation signal and then divide each term by the power spectral density of the excitation signal. The result is:

$$
\begin{aligned}
H_x &= H_{xo} - \varepsilon_{xy} H_{yo} - \varepsilon_{xz} H_{zo} \\
H_y &= -\varepsilon_{yx} H_{xo} + H_{yo} - \varepsilon_{yz} H_{zo} \\
H_z &= -\varepsilon_{zx} H_{xo} - \varepsilon_{zy} H_{yo} + H_{zo}
\end{aligned} \tag{11}
$$

or

$$
\begin{Bmatrix} H_x \\ H_y \\ H_z \end{Bmatrix} = \begin{bmatrix} & \varepsilon & \end{bmatrix} \begin{Bmatrix} H_{xo} \\ H_{yo} \\ H_{zo} \end{Bmatrix} \tag{12}
$$

where H_i = $H_i(\omega)$ is the FRF for the true structural motion in the ith direction

H_{io} = $H_{io}(\omega)$ is the apparent FRF with contaminated information about the structures motion in the ith direction.

i = x, y, and z.

Equation (11) or (12) is attractive to use since the calculations to remove the cross-axis contamination are performed on the averaged FRFs. This fact significantly reduces the required calculations. In addition, Eq. (11) or (12) simply requires that the FRFs be obtained simultaneously. No cross spectral calculations between the structural responses are required. This is a decided advantage over Eq. (10) which has a large number of such cross spectral terms. Hence, several dual channel FFT units can be used to obtain the FRFs for Eq. (11) or (12) where the excitation is a common signal to each dual channel unit.

III. EXPERIMENTAL PROCEDURE

A. Accelerometer Calibration in Time Domain

Two different triaxial accelerometer units were calibrated and used in this experiment. One is a triaxial accelerometer manufactured by PCB (Model 306A06). The other triaxial accelerometer was constructed by mounting three Endevco (Model 2222) miniature accelerometers on a 15.88mm X 15.88mmm X 15.88mm steel cube with ground parallel and perpendicular surfaces. The relative position of each accelerometer was maintained throughout the entire experimental procedure from calibration to actual acceleration measurement to ensure consistent transducer characteristics in sensing cross-axis motion.

In order to measure the sensitivity of a transducer, it is first necessary to define the absolute motion of the calibration shaker. It is obvious that any amount of transverse motion in the shaker will deteriorate the cross-axis calibration results, since any transverse motion generates a signal output due to the primary sensitivity of the transducer which has much higher value than the cross-axis sensitivity. Therefore, only a small amount of transverse motion in the shaker can generate almost the same order of erroneous signal as that of the signal to be calibrated. There are several methods to determine the absolute motion of the shaker. One method uses two noncontacting mutual-inductuance probes [7] to measure the motion. In a method used by the National Bureau of Standards [8] in evaluating vibration

standards, three accelerometers with nearly equal sensitivities are mounted with their principal sensitivity axes mutually perpendicular to each other as in this experiment. Once the absolute motion of the shaker is defined, transverse calibrations of transducers are best performed within the frequency range where errors resulting from extraneous transverse motion are small.

For this experiment, a specially constructed calibrator as shown in Fig. 4 is used to measure the 9 voltage sensitivities. The main feature of this calibrator is to provide uniaxial motion of mounted accelerometers and to minimize interference of the supporting structure. It consists of a guide shaft and a teflon bearing. A steel shaft of circular section with 3/4" diameter and 4 1/2" long is used as the guide shaft. The calibration standard accelerometer is attached to one end of the shaft and the impact head is attached to the other end of the shaft. The triaxial accelerometer is attached to the calibtation standard as shown in Fig. 4. The impulse duration is controlled by the impact head. The teflon bearing is 3" long and rigidly connected to the ground floor to provide fixed position relative to the motion of the guide shaft when impacted. The clearance between the shaft and bearing is 8/10000" so that the guiding shaft can undergo smooth linear motion without yawing and pitching. The impact pendulum is suspended from the ceiling and its motion is restricted to the vertical plane. The pendulum support is carefully aligned to ensure that the tangential direction of the circular path coincides with the longitudinal axis of the guide shaft at the moment of impact. This calibration impulse excitation technique is

consistent with the structural test procedure that also uses an impulsive excitation.

The nearly half sine impulse signal from each transducer and a standard calibration accelerometer are recorded simultaneously on a Norland 3001/DMX digital processing oscilloscope. The calibration accelerometer has a sensitivity of 10.0 mV/g over a broad range of frequencies. The sensitivity of each transducer is obtained by plotting the output of the transducer to be calibrated (either a primary or a cross-axis direction) on the vertical axis against the standard signal on the horizontal axis of the digital oscilloscope Cathode Ray Tube (CRT). The signal relationship should be that of a straight line. An internal statistical program is used to calculate best straight line parameters from the data as well as the corresponding correlation coefficient bewteen the two signals. Then, the sensitivity of transducer i in direction j is given by

$$S_{ij} = 10.0\ b_j \quad (\text{mV/g}) \tag{13}$$

where b_j is the slope of the line. The results of this test are presented in Table 1 where the slopes and correlation coefficients (in parentheses) are shown. The negative slopes indicate that the cross-axis output was 180^{o} out of phase with respect to the standard impulse signal.

One of the major problems with this calibration scheme is to remove any cross-axis motion of the rod in its teflon bearing. Some

calibration runs had to be repeated since the cross-axis signal clearly showed significant motion. Careful alignment of the impact bar and sufficient lubrication between the rod and teflon bearing tended to reduce these problems. Typical time history plots of signals from primary sensing axis and cross-axis of each Endevco miniature accelerometer constructed for a triaxial accelerometer for a appropriate time window are shown in Fig. 5. In Fig. 5, a_{xx} is the signal from the accelerometer with the primary sensing axis in the x-direction, a_{yx} is from the accelerometer with the primary sensing axis in the y-direction, and a_{zx} is from the accelerometer with the primary sensing axis in the z-direction. The second subscript x indicates the direction of input impulse. The time history a_{xx} is a smooth and nearly complete half sine wave as expected, while a_{yx} and a_{zx} have higher frequency components superimposed. These higher frequency components can be related to the first natural frequency of the guide shaft in a flexural mode and the natural frequency of the support structure, which are around 190 Hz and 310 Hz, respectively. To eliminate the effect of extraneous transverse motion of the calibrator on the calibration results, succeeding measurements with this triaxial accelerometer were restricted to an upper limit of 50 Hz. The calibration data given in Table 1 was used for the compensation scheme on the FRFs of the zoom measurement. Nine elements of the normalized sensitivity matrix in Table 1 represent constant sensitivity values in this frequency range.

B. Accelerometer Calibration in Frequency Domain

The level of signals generated by cross-axis sensitivity is small compared with that of the primary sensing axis signal. Hence, any slight deviation of the calibration set-up from uniaxial motion gives a poor cross-axis signal that is contaminated by the dominant primary axis signal. The calibration scheme must be adequate to compare the relatively low level of the cross-axis signal with the high level of the primary sensing axis signal. In addition, it must detect any possible overlap of high level signal onto a low level one. The calibration method using a resonant bar satisfies these requirements.

A beam of rectangular cross section was constructed as a test structure for use in calibration. This beam is similar to that used for the modal analysis. Detailed dimensions of the resonant beam and primary and cross-axis directions are shown in Fig. 6. The beam is supported at those node points which correspond to the fundamental free-free mode of vibration. The standard accelerometer and the triaxial accelerometer that is to be calibrated are mounted at the midpoint of the beam. When the beam is excited by an impulse applied at its midpoint, a relatively high level of response occurs at the first and third free-free natural frequency of the beam. The standard accelerometer signal is considered to be the input while the output signal corresponds to the accelerometer that is being calibrated. The required transducer sensitivity ratio is determined from the frequency response function over a narrow range of frequencies around each natural

frequency. The frequency resolution is increased by using the zoom analysis around each resonant frequency. Since the resonant bar has close natural frequencies in each direction perpendicular to the rectangular cross section, any signal overlap from the primary sensing axis due to a deviation from a unidirectional response can be detected as an additional peak in the zoomed power spectral density measurement for the cross-axis signal.

The zoomed cross-axis output for the x-direction is shown in Fig. 7 with the frequency ranging from 140 to 190 Hz. The third natural frequency of the beam is about 164.6 Hz which lies near the mid point of the frequency axis shown. The reference signal used for both the FRF and the coherence function is the standard reference accelerometer signal. The frequency response function is flat with a constant value over a narrow range of frequencies around the third natural frequency of the beam. The corresponding coherence function has value close to 1 which is required to have a reliable measurement of the sensitivity ratio from the FRF. The low value of the coherence function in the region away from the resonance frequency indicates that a significantly lower level of transducer signal is being obtained. In other words, the noise to signal ratio off the resonant frequency is significantly high. Therefore, the information contained in the frequency response function may be contaminated and is not reliable for this frequency range. These results suggest that calibration of the cross-axis signal should be restricted only at specific frequencies corresponding to the natural frequencies of the resonant bar where relatively high level of responses

are obtained.

Figures 8 and 9 show the zoomed and baseband frequency response functions and coherence functions between the standard signal and one of the primary sensing axis signal, respectively. Both figures show a high value of the coherence function for a relatively broad range of frequency, which demonstrates acceptability of this calibration scheme for the primary sensing direction. A principal disadvantage of this calibration method is that only the resonant frequencies of the beam can be used. By using several beams with different cross sections, a number of discrete points can be plotted over a desired range of frequencies. A curve can be drawn through these points to show how the calibration varies with frequency.

The PCB triaxial accelerometer calibration results are given in the form of a sensitivity matrix in Table 2. This calibration data will be used in the compensation scheme for the baseband measurement of frequency response functions.

C. Impact Hammer Calibration

A standard PCB Model 086B09 impulse force hammer is used to excite the beam. Various impact tips are tested to obtain the desired impulse time duration. Two impulse time durations are required in this experiment. One is around 2 msec for the baseband measurement up to 200 Hz, and the other is around 20 msec for the zoom measurement with frequency band of 50 Hz. The mass of the impact tip and hammer body

greatly effects the sensitivity of force transducer instrumented on the hammer [9][10][11]. Therefore, the impact hammer should be calibrated for each different impact tip being used. A pendulum system is used for the calibration of the impact hammer, whose detailed procedure is described in Reference [11]. An acrylic tip is used to provide 2 msec impact duration. The calibrated sensitivity of the force transducer with this tip is 10.0 mV/lbf. The other time duration of 20 msec is obtained by attaching soft rubber tip, which gives sensitivity of 10.3 mV/lbf.

D. Vibration Measurement

1. Experimental apparatus

A uniform rectangular, nearly square, cold rolled steel beam is used as a test structure. The bar dimensions and coordinate system are shown in Fig. 10. The beam is discretized with 24 nodal points along the length of the beam in the x-direction. The cross section dimensions are chosen in such a manner that the natural frequencies in the y and z directions are closely spaced for each free-free mode of vibration. The frequency ratio of the corresponding modes in y and z-direction is the ratio of the dimensions of beam cross section; that is $y/z = 9/8$. This ratio gives approximately a 3 Hz difference for the first mode and a 30 Hz difference for the fourth mode. Theoretical values of natural

frequencies of the test beam calculated using the Euler beam theory are shown in Table 3.

The beam is suspended by soft cords at the two node points for the fundamental free-free mode of vibration as shown in Fig. 10. It is desired to provide consistent positional and directional force input to the beam. In order to provide consistent positional inputs, small cone shaped dents are spaced along the x-axis on both y and z surfaces. A small steel ball is placed in the dent and is held in position by using beeswax. When the ball is actually hit by the impact hammer, the location of the input is precisely controlled with this scheme. A consistent impact direction remains the only major problem in striking the beam.

Two cases of impact direction are considered in this experiment. In the first case, the beam is impacted in the y-direction. The intent is to excite only motion in the y-direction so that (a) contamination in the other direction is clearly evident and (b) the true frequency response function in the y-direction is obtained with minimum error.

In the second case, the excitation is applied at the corner of the beam at an angle of 42^{o} (arctan 8/9) from the y axis along the S-direction as shown in Fig. 10. This type of excitation, which has same effect of giving input in both y and z-direction, is considered to produce a clear example of contaminated frequency response functions in both y and z-direction. Furthermore, since the input direction passes through the shear center of the beam cross section, the torsional mode of the beam is effectively removed. This is called the S-direction

input. In this case, the beam is rotated 42^{o} so that S-direction is then horizontal and is perpendicular to the supporting cords. This rotation helps to keep the impact directions more precisely aligned.

The calibrated triaxial accelerometer is attached at the positive x-direction surface of the beam. Each accelerometer output is connected to one of three Bruel & Kjaer (B&K) type 2032 dual channel signal analyzers. When measuring transient responses in order to obtain the corresponding FRF for the three directions, all analyzer units should trigger at approximately the same instant. Thus, all analyzer units use the same force transducer sensitivities and voltage trigger levels. When time domain corrections are used, a four channel system using simultaneous sampling is required. Thus, frequency domain method in which each individual FRF is employed has an additional advantage.

2. Frequency analyzer description

The analysis on the Bruel & Kjaer (B&K) dual channel signal analyzer type 2032 is performed using the Fast Fourier Transformation (FFT) algorithm of the Discrete Fourier Transformation (DFT) which works on blocks of time data. Several different types of weighting functions can be applied to the time history records before the FFT is calculated on each channel. Also the type of averaging (linear or exponential) and the number of averages can be selected according to the type of analysis.

For this experiment, two different weighting functions are applied

on each channel. A transient window function is applied to the force signal in channel A, which will increase the signal to noise ratio and exclude other force signals which are not fed into the structure. Exponential window function is applied to the response signal (acceleration) in channel B in order to avoid leakage effects due to truncation of the signal at the end of the record and in order to increase the signal to noise ratio in the analysis.

There are two types of frequency response functions defined in B&K type 2032 signal analyzer [12][13]. These are:

$$H_1(f) = \frac{G_{AB}(f)}{G_{AA}(f)}$$
$$H_2(f) = \frac{G_{BB}(f)}{G_{BA}(f)} \qquad (14)$$

where G_{AA} is Power Spectral Density function of input

G_{BB} is Power Spectral Density function of output

G_{AB} and G_{BA} are Cross Spectral Density functions between input and output.

For an ideal situation in which the measured signals are not contaminated by any kind of extraneous noise, H_1 and H_2 are identical. If the measured input signal is contaminated by extraneous noise, H_2 gives unbiased estimation of the frequency response of the system. On the other hand, H_1 gives the unbiased estimation of the frequency response when the measured output signal is contaminated by extraneous noise. Generally, H_1 is used for the notches, where output noise tends

to dominate, and H_2 at the peaks, where input noise or leakage tends to cause the problem.

For the data analysis in this experiment, H_1 is chosen as the estimated FRF of the test beam. The reasons are (a) the output signal from the cross-axis of the accelerometer is most susceptible to noise, (b) the zoom measurement that is taken where resolution bias error causes the problem would improve the estimation, and (c) the window functions applied play a role of idealizing the input and output, thus H_1 and H_2 are almost identical each other with this measurement set-up.

The FRF is obtained by averaging 10 sets of input-output data for each input location. A standard linear averaging scheme is utilized where each FRF carries the same weight.

The standard computer program used to extract modal parameters is the Modal-Plus 9.0 software developed by Structural Dynamics Research Corporation (SDRC). This program is designed to process only 512 spectral lines of the frequency response function. Therefore, even though B&K type 2032 signal analyzer generates 801 spectral lines to represent frequency response function for a given frequency window, only 512 spectral lines of the measurement are stored in the computer for later analysis.

3. Baseband measurement

Baseband measurement of the frequency response function can provide an overall view of the test structure for relatively broad range of

frequencies. The PCB triaxial accelerometer, which was calibrated using the resonant bar technique is used for this measurement. The frequency range of these measurements is 0~400 Hz with resolution of 0.5 Hz. This frequency range includes four natural modes of the test beam.

The impact duration is about 2 msec, so that most input energy is concentrated in the frequency range below 400 Hz. FRF values from 10.5 Hz to 266.0 Hz which corresponds 512 spectral lines are stored in the computer for the reason stated above. The low frequency region is dropped out to eliminate DC drifting of the instruments and rigid body modes of the test beam.

4. Zoom measurement

The advantage of zoom measurement is that it can provide greater detail of the frequency response function over a narrow frequency range that is of interest. Furthermore, frequency resolution bias error can be significantly reduced with zoom measurement, especially for a lightly damped structure like the test beam used in this experiment.

The triaxial accelerometer, which was constructed using 3 miniature Endevco accelerometers, was used for the zoom measurement. Since the calibration data for this triaxial accelerometer is reliable only below 150 Hz, zoom measurement around the first natural frequency of the beam was considered. For this measurement, the center frequency is 25 Hz with bandwidth 50 Hz and frequency resolution of 0.0625 Hz. For the same reason as in the baseband measurement, only 512 spectral lines (5.0

~ 36.9375 Hz) are stored for data analysis.

Except the frequency resolution, all measurement settings are identical with the baseband measurement.

IV. RESULTS AND DISCUSSION

A. Frequency Response Functions with Baseband Measurement

Figures 11 and 12 are the frequency response functions (FRFs) of the test beam obtained from simultaneously measured signals of accelerometers with primary sensing axes in the y and z-direction when the input is in the S-direction. These are typical FRFs when the response coordinate and excitation coordinate are identical at node 1 of the beam. They are characterized by their deep troughs between the resonant peaks. Figures 13 and 14 are typical transfer FRFs when the response coordinate is at node 1 and the input coordinate is at node 24 at the extreme end of the beam. The direction of input and output are the same as in Figs. 11 and 12.

In Figs. 11 and 13, points B, C and D indicate the clear evidence of parasitic peaks due to the z-directional bending modes of the beam sensed by the cross-axis sensitivity of the accelerometer with the primary sensing axis in the y-direction. Similarly, in Figs. 12 and 14, points A, B, C, and D indicate the amount of contamination due to the y-directional bending modes of the beam sensed by the cross-axis sensitivity of the accelerometer with the primary sensing axis in the z-direction.

In each of these figures, the additional peak at point A which corresponds to the parasitic first mode of the test beam in either y-direction or z-direction is not as significant as the other parasitic

peaks are at points B, C, and D. This suggests that the 0.5 Hz frequency resolution is inadequate to clearly identify these two peaks which are spaced about 3 Hz apart. This question of frequency resolution is explored in the next section when zoom measurements are made around the fundamental frequency with a resolution of 0.0625 Hz.

The main feature of these additional peaks is that each peak is preceded or followed by a deep crest, especially for Figs. 13 and 14 in which there should be no troughs for typical transfer FRFs. This phenomenon can be explained as follows. The normalized mode shapes are identical both in y and z direction for the one dimensional beam. Therefore, the modal constants of these parasitic modes have the same sign as those of corresponding true modes. If two consecutive modes have the same sign for the modal constants, the contributions of the two modes have opposite sign to each other so that they are subtractive in the region between the two resonances. This small value of frequency response produces the anti-resonance characteristic on a logarithmic plot of these types. The most important feature of the antiresonance is the fact that there is a phase change associated with it, as well as a very low magnitude. This sudden phase shift will effect the modal parameters to be extracted significantly when the circle-fit methods are used [14].

Figures 11, 12, 13 and 14 demonstrate the results of compensation on the contaminated FRFs. The compensated curve not only effectively removes the additional peaks but also reflects the scale factor correction for the true FRF in each direction. The difference in

magnitude of raw and compensated FRF is due to the scale factor of the inclined input. The input in the S-direction is the vector sum of the components in pure y and z-directional input. This means that the raw FRF, with an input in the S-direction, gives underestimated frequency response of the beam in y and z-direction by the scale factor of 0.44 [= $\sin^2(\arctan 8/9)$] and 0.56 [= $\cos^2(\arctan 8/9)$], respectively.

It is necessary to examine if these compensated FRFs actually represent the true FRFs of the test beam. This is done by conducting a set of measurements where the input force is in the y-direction only. For this input case, the cross-axis sensitivity will have a minimum effect on the y-direction output, so that the resulting FRF can be considered to be the true y-direction bending mode. Figures 15 and 16 show the FRFs of the beam in y-direction with input in the y-direction at node 1 and 24 which are compared with the compensated FRFs of Figs. 11 and 13. Except for the discrepancies around troughs, where the signal level is extremely low, the two FRFs match well. Since the most important region for analysis is usually around the peaks, the compensation scheme is considered to effectively retrieve the true FRF of the test beam.

An interesting feature of the cross-axis sensitivity effect on the measured FRF is illustrated in Fig. 17. In this figure, the FRF of the beam in the y-direction with an S-direction input at node 3 is shown. The node number 3 is close to the nodal point of the third natural mode of the test beam. Here, the additional peak at point A which corresponds to the third natural frequency of the beam in the

z-direction appears insignificant. This indicates that the effect of the cross-axis sensitivity is not significant, unless the response of the structure in that particular cross-axis direction is significant. Compensated FRF compared with FRF in the y-directional input and output is also shown in Fig. 18, demonstrating the effectiveness of this compensation scheme.

B. Frequency Response Functions with Zoom Measurement

Figure 19 shows the averaged raw and compensated FRF (magnitude and phase) for the y-direction when the beam was impacted in the y-direction. This is a nearly ideal situation for many reasons. First, a perfect impact should excite only y-direction motion. Second, the primary sensing axis of the transducer is in the direction of dominant motion. Thus, the raw and compensated FRFs are nearly identical. The modal analysis software is designed to analyze this type of data.

Figure 20 shows the raw and compensated FRF in the x-direction when the beam was impacted in the y-direction. In the region around point A, there is no response above the measurement system noise threshold because of the low-level response in the z-direction. At point B, however, there is a significant cross-axis transducer response to the motion induced in the y-direction by the impact in the y-direction. The compensated technique effectively removes this sensitivity to nearly the same level as the measurement system noise threshold.

Figure 21 shows the raw and compensated FRF in the z-direction when

the beam is impacted in the y-direction. The peak at A is due to the small amount of motion that is induced in the z-direction because of an imperfect test system. This imperfection is caused by impact hammer misalignment and nonorthogonality of the physical system. Figure 21 also shows how the compensation effectively removes the y-axis response at point B, reducing the signal to the noise threshold, while there was no significant change in peak A.

Figure 22 shows the raw and compensated FRF in the x-direction when the beam is impacted in the S-direction. The x-axis transducer is sensitive to both the y-axis and the z-axis motion as shown at points A and B. The compensation removes most of this cross-axis sensitivity and gives a signal that represents the noise threshold for this accelerometer system.

Figure 23 shows the raw and compensated FRF in the y-direction when the beam is impacted in the S-direction. The S-direction impact excites large responses in both the y and z-directions. The transducer sensitivity to the z-direction acceleration is shown by the dual peak pair at points A and B. The compensation removes most of this contaminated information, and the resulting curve is identical to that shown in Fig. 19 for the nearly ideal response FRF except for the scale factor due to the angle of impact.

Figure 24 shows the raw and compensated FRF in the z-direction when the beam is impacted in the S-direction. The z-axis transducer is sensitive to the y-axis motion as shown at points A and B. The compensation removes this contaminated information.

C. Modal Parameters Extracted

The most important question from the engineering point of view is what is the effect of the transducer cross-axis sensitivity on the final results obtained from the measured frequency response functions (FRFs). In other words, are those parameters which are to be extracted from the contaminated FRFs significantly different from those obtained from the true FRFs of the structure, or are the errors negligible and can be neglected?

To answer this important question, two sets of FRFs for the test beam are analyzed by the modal analysis software. The first set consists of the raw FRFs obtained using signals from the accelerometer with its primary sensing axis in the y-direction with the S-direction input. The second set consists of the compensated FRFs shown in Figs. 11, 12, 15 and 16.

Figure 25 is the plot of Bode diagram corresponding to the raw FRF of Fig. 11 which is the baseband measurement at node 1 and its equivalent analytical model generated by Modal-Plus using the search peak algorithm [15]. Modal-Plus extracts modal parameters by the repeated application of an single degree of freedom curve-fit to each of the resonances in turn until all modes visible on the plot have been identified. An analytical curve, based on the modal parameters extracted from the measured data, is overlaid on the original measured curve to assess the success of the curve-fitting process. If the

measured and analytically generated FRFs match well, this indicates the analysis is successful. According to the result shown in Fig. 25, the program identifies the parasitic peaks as true natural modes of the beam. An exception is the first small peak that occurs just before the first large peak which is lost due to the large Δf of the frequency analysis. The appearance of the parasitic peaks leads the program to identify 7 natural frequencies for the test beam in this frequency range, while only 4 of them are true natural frequencies. In addition to those fictitious natural frequencies, these peaks deteriorate the overall shape of the FRF and significantly effect the other parameters to be extracted, especially when using a multi-degree of freedom algorithm [15].

Figure 26 shows the compensated FRF from Fig. 11 and its analytical model. This gives 4 natural frequencies of the beam in the y-direction which is consistent with the beam model for this frequency bandwidth.

Modal parameters are extracted from three different data sets and they are given in Tables 4, 5, and 6 for comparision. In these tables, YY represents the case considered as true modal parameters that are extracted from the FRF in Fig. 15 with both the input and output in the y-direction. The heading SY corresponds to the FRF in Fig. 25 with the input in the S-direction and contaminated output in the y-direction. The heading CS corresponds to the FRF in Fig. 26 in which the contamination is compensated for.

In Table 4, three sets of natural frequencies are compared. In case YY, the four frequencies extracted are reasonable estimates of the

natural frequencies of the test beam given in Table 3. Each frequency extracted is a little lower than its corresponding theoretical value. One reason is that the extracted frequencies are damped natural frequencies which are slightly lower than undamped natural frequencies. A second reason is that the calculated natural frequencies are based on the Euler beam theory which ignores shear deformation and rotary inertia effects. A completely different result is shown in case SY. Three additional modes are extracted compared to the case YY. The extraction of each natural frequency is based on the actual peaks shown in the FRF plot. These three parasitic modes are different from the so called 'computational modes' which often appear when the complex exponential algorithm is used to extract natural frequencies. It is obvious that this type of analytical result can mislead even an experienced analyst. Real physical modes of the test beam are clearly retrieved in case CS after compensation. The beauty of the compensation scheme is that it is not necessary to apply any engineering judgement to interpret the test results to identify the real modes.

In Table 5, three sets of modal damping values are compared. Unfortunately, there is no way to compare these experimental values with corresponding theoretical ones. Actually, it is the main feature of the experimental modal analysis that the damping, which is often a troublesome quantity to estimate with an analytical approach, can be directly estimated from the measured structural response. A comparison of the two cases, YY and SY, reveals that the damping value is generally underestimated for the contaminated FRF. This general trend can be

explained by examining the overall shape of the FRF in Fig. 25. To curve-fit all the parasitic peaks, the overall shape of the FRF is inevitably distorted which makes the peaks appear sharper than they actually are. The estimated damping value based on the shape of FRF around the resonant peak naturally becomes smaller. Also it is interesting to note that the damping values of the second and fourth modes in the SY case are significantly smaller than the others. These are the damping values of the parasitic modes, and again are enough to confuse the analyst. Usually, the analyst examines the damping values in order to identify the fictitious 'computational modes', because the computational modes have significantly higher damping values than those of the true modes. The correspondingly small damping values in the SY case are just another example illustrating how difficult it is to recognize the cross-axis sensitivity error during the analysis stage. Conversely, the compensated FRF in the CS case gives nearly the same values for the estimated modal damping of the test beam as in the YY case.

In Table 6, three sets of modal constants are compared. Modal constants are the basic quantity which estimate the mode shape of the test structure. It is not surprising to note that the modal constants in the SY case are much less than those in YY case, considering the scale factor of the input force. Again, the parasitic modes have significantly lower values for modal constants. Since the modal constant is an index of the modal contribution to the structural response, the amount of error due to the cross-axis sensitivity of the

transducer can be easily seen in this table. The compensated FRF provides nearly the same modal constant as that obtained in the YY case. The greatest error, however, occurred in the first mode. The relatively large discrepancy that occurred in the first mode between cases YY and CS is considered to be due to the resolution bias error around the first peak where the parasitic peak and the real peak are mixed together.

Figures 27 shows the analytical model for the contaminated FRF around the first mode from the zoom data, while Fig. 28 shows the corresponding analytical model for the compensated FRF. A comparison of these figures shows the significant effect of the cross-axis sensitivity on the parameters to be extracted.

D. Mode Shapes

It is possible to extract certain modal properties for a particular mode by curve-fitting a single FRF curve. This curve-fitting procedure gives the natural frequencies and damping properties directly. But it does not explicitly yield the mode shape. In order to extract mode shapes, it is necessary to measure and analyze a full set of N FRFs for an N degree of freedom structure. The fact that the cross-axis sensitivity of the accelerometer contaminates the entire set of measured FRFs for a given input and output direction is best illustrated by the mode shapes calculated.

Figure 29 shows the first mode shape of the beam in the y-direction where the contaminated FRFs and compensated FRFs produce identical

shapes. These two mode shapes are indistinguishable, even though the modal constants estimated from each FRF at node 1 are different as shown in Table 6. It can be shown that the relative ratios not the absolute values of the modal constants which are estimated from two different sets of FRFs, are identical to each other at the corresponding nodes. In Fig. 30, however, the second and third mode shapes calculated from the contaminated FRFs produce almost identical mode shapes, while the third contaminated mode shape appears identical to the second mode shape calculated from the compensated FRF data. Actually, the second mode shape MS2Y2 in Fig. 30 corresponds to the second mode shape of the beam in the z-direction which supposedly gives an identical mode shape when normalized. This result indicates that the transducer cross-axis sensitivity error is nearly proportional to the response of the beam in the z-direction among the entire set of FRFs measured, and is not restricted to a particular FRF. Since the test beam in this experiment has identical mode shapes in both y and z direction, the erroneous mode is relatively easy to recognize. But it is obvious, when the test structure has different mode shapes in 3-dimensions, that this kind of confusion can result in misleading information on the true mode shapes of the structure at various frequencies.

Figures 31 and 32 show the fourth and fifth as well as the sixth and seventh mode shapes that are calculated from the contaminated FRFs. These are compared with the true third and fourth mode shapes of the beam that are calculated from the uncontaminated YY FRF data, respectively. All these figures show that the transducer cross-axis

sensitivity can systematically contaminate the measured response. The amount of contamination and error depends on the response in the particular direction that is measured as well as the direction perpendicular to the primary sensing axis of the transducer.

V. CONCLUSIONS AND RECOMMENDATIONS

The effects of transducer cross-axis sensitivity on experimental modal analysis are investigated in this research. The cross-axis sensitivity is an inherent characteristic of the transducer, and it ranges from about one to five percent for the transducer employed in these experiments. In each transducer tested, the cross-axis sensitivity effects were evident in the test data when displayed in the frequency response function form.

The experience of using contaminated transducer signals in an experiment designed to clearly show the cross-axis sensitivity effects supports the following conclusions.

1. The proposed theoretical input-output model that is developed from Eq. (1) is an adequate representation of the cross-axis sensitivity effect of the transducer. This model shows that nine transducer voltage sensitivities are required to completely define a tri-axial transducer.
2. The error due to the cross-axis sensitivity of transducer cannot be neglected whenever there is a directional misalignment between the structural response and the primary sensing axis of the transducer used.
3. The cross-axis sensitivity effects are clearly evident in the FRF for a given primary sensing direction for this well defined demonstration structure. This result shows that the cross-axis contamination error is not random in nature. This

error is systematically accumulated in the averaged FRFs.

4. The cross-axis error can be effectively removed in the frequency domain by using the simple approximated equations given as Eqs. (11) and (12). The equations rely only on the normalized cross-axis sensitivities ε_{ij}.
5. The ability to correct the FRFs after averaging the experimental data is computationally efficient.
6. The modal parameters, consisting of natural frequency, damping, modal constant, and mode shape, are distorted and often incorrect when the contaminated FRFs are used in the data analysis. This distortion is shown in Tables 4, 5, and 6.
7. The modal parameters obtained from the corrected FRFs which includes cross-axis effects are nearly identical to those obtained from the ideal input case which exhibited no cross-axis effects. This can also be seen in Tables 4, 5, and 6.

One of the major applications of experimental modal analysis is to verify the validity of a finite element or other theoretical model. The distorted modal parameters obtained from the uncorrected FRFs can have far reaching effects when trying to match finite element or other theoretical results to experimental results. Often the theoretical models are distorted or made incorrect in order to match the incorrect experimental data. Therefore, it is recommended that any modal test for a structure that is suspected of coupled modes, which is not uncommon in practice, should utilize this correction procedure in order to obtain an

accurate vibration response model.

A major problem in this correction scheme is to accurately determine the six cross-axis transducer sensitivities in a tri-axial accelerometer. These sensitivities represent the signal due to a pure motion in a direction parallel to one of the primary sensing axis of the tri-axial accelerometer. Any motion other than the primary sensing direction severely contaminates the calibration results. Thus, it is recommended that a better and easier to use calibration scheme be developed that will allow the cross-axis sensitivities to be obtained over a broad range of frequencies. Such a calibration scheme is crucially needed in order to make this correction technique economically available to the testing industry.

VI. BIBLIOGRAPHY

1. Ewins, D. J. Modal Testing: Theory and Practice. Letchworth, Hertfordshire, England, Research Studies Press Ltd., 1984.
2. Craig, R .R., Chung, Y. T. and Blair, M. "Modal Vector Estimation for Closely-Spaced Frequency Modes." Bureau of Eng. Research, The Univ. of Texas at Austin, Report AR 82-1, 1982.
3. Hallauer, W. L. and Stafford, J. F. "On the Distribution of Shaker Forces in Multiple-Shaker Modal Testing." Shock and Vibration Bulletin, Bulletin 48 (Part 1) (Sept. 1978), 49-63.
4. Hallauer, W. L. and Frank, A. "On determining the Number of Dominant Modes in Sinusoidal Structural Response." Shock and Vibration Bulletin, Bulletin 49 (Sept. 1979), 19-34.
5. Komrower, J. M. and Pakstys, M. P. "Verification of Modal Testing and Analysis Techniques for Predictions of Dynamic Strain in Impact Loaded Structures." Proceedings of 2nd International Modal Analysis Conference, Feb. 1984, 620-626.
6. Crowley, S. M. and Allemang, R. J. "Applications of the Poly Reference Technique in Experimental Modal Analysis." Proceedings of 2nd Internatinal Modal Analysis Conference, Feb. 1984, 111-117.
7. Elliot, W. R. Proc. Instr. Soc. Am., 10, Part 2, Paper 55-21-1, 1955.
8. Bouche, R. R. "Improved Standard for the Calibration of Vibration Pickups." Proc. SESA Paper 570, May 1959.
9. Halvorsen, W. G. and Brown, D. L. "Impulse Technique for Structural

Frequency Response Testing." Sound and Vib. (November 1977), 8-21.

10. Dally, J. W. and Riley, W. F. and McConnell, K. G. Instrumentation for Engineering Measurements. New York: John Wiley & Sons, Inc., 1984.
11. McConnell, K. G. and Han, S. B. "Effect of Mass on Force Transducer Sensitivity." Exp. Tech., 10(7) (1986): 19-22.
12. Bendat, J. S. and Piersol, A. G. Engineering Applications of Correlation and Spectral Analysis. New York: John Wiley & Sons, 1980.
13. Bruel & Kjaer Inc. "To Advance Techniques in Acoustical, Electrical and Mechanical Measurement." Bruel & Kjaer (Marlborough,Mass.) Technical Review 1 (1984): 1-57.
14. Stroud, R. C. "Excitation, measurement, and Analysis Methods for Modal Testing." Sound and Vibration (August 1987): 12-27.
15. User Manual for Modal Analysis 9.0 , General Electric/SDRC company 1985.
16. Meirovitch, L. Analytical Methods in Vibrations. London, England, The Macmillan Company, 1967.
17. Richardson, M. and Potter, R. "Identification of the Modal Properties on an Elastic Structure from Measured Transfer Function Data." ISA ASI 74250. Proceedings of the 20th International Instrumentation Symposium, 20 (1974): 239-246.
18. Coppolino, R. N., Ibrahim, S. R., Hunt, D. L. and Stroud, R. D. "Advanced Methods Used on the Galileo Spacecraft Modal Survey." Proceedings of 2nd International Modal Analysis Conference (Feb.

1984), 813-819.

19. Richardson, M. H. and Formenti, D. L. "Parameter Estimation from Frequency Response Measurements Using Rational Fraction Polynomials." Proceedings of 1st International Modal Analysis Conference (Nov. 1982), 167-181.

20. Allemang, R. J. "Experimental Modal Analysis." ASME AMD, 59 1-29.

21. Harris, C. M. and Crede, C. E. Shock and Vibration Handbook. Engineering Design and Environmental Conditions New York: McGraw-Hill, 1976.

22. Endevco Corporation. "Instruction Manual for Endevco Piezoelectric Accelerometers" Endevco Corp., California, 1979.

VII. ACKNOWLEDGMENTS

I would like to express my gratitude to Dr. Kenneth G. McConnell, my major professor, for his advice and guidance throughout the course of this study. This research work was accomplished very effectively due to his valuable insight and suggestions. I enjoyed my experience of working with him, for I always learned something from our contact.

Also, I would like to thank Mr. T. Elliot for his help with the laboratory work.

I wish to thank my mother and family in Korea who understood and supported me while studying abroad.

Also, I want to thank my wife Sung-Jin who accompanied me in those long and hard days to see the outcome of this work.

VIII. TABLES AND FIGURES

Table 1. Normalized sensitivity matrix $[\varepsilon_{ij}]$ obtained using calibrator for the triaxial accelerometer constructed by three Endevco miniature accelerometers
(Numbers in parentheses are linear correlation coefficients with respect to the standard calibration signal)

1.000 (0.99)	0.008 (0.85)	-0.028 (0.92)
-0.041 (0.94)	1.000 (0.99)	0.041 (0.96)
-0.016 (0.84)	-0.020 (0.91)	1.000 (0.99)

Table 2. Normalized sensitivity matrix $[\varepsilon_{ij}]$ obtained using resonant bar for the triaxial accelerometer PCB Model 306A06

1.000	0.028	-0.051
-0.045	1.000	0.041
0.020	-0.036	1.000

Table 3. Natural frequencies of the test beam in three directions

direction / mode	x	y	z
First	1099 Hz	27.63 Hz	24.56 Hz
Second	2198 Hz	76.17 Hz	67.71 Hz
Third	3298 Hz	149.34 Hz	132.75 Hz
Fourth	4396 Hz	246.84 Hz	219.42 Hz

Table 4. Natural frequencies extracted from 3 different sets of FRF

Mode	YY[a]	SY[b]	CS[c]
1st	27.58 Hz	27.59 Hz	27.59 Hz
2nd	75.86 Hz	67.55 Hz	75.91 Hz
3rd	148.41 Hz	75.91 Hz	148.52 Hz
4th	244.92 Hz	132.29 Hz	244.92 Hz
5th		148.52 Hz	
6th		218.05 Hz	
7th		244.92 Hz	

[a]FRF with both input and output in the y-direction.

[b]FRF with input in the S-direction and output in the y-direction.

[c]FRF compensated from the case SY.

Table 5. Modal damping values extracted from 3 different sets of FRF

Mode	YY[a]	SY[b]	CS[c]
1st	0.00560	0.00401	0.00501
2nd	0.00154	0.00008	0.00143
3rd	0.00131	0.00142	0.00122
4th	0.00056	0.00038	0.00060
5th		0.00073	
6th		0.00068	
7th		0.00070	

[a]FRF with both input and output in the y-direction.

[b]FRF with input in the S-direction and output in the y-direction.

[c]FRF compensated from the case SY.

Table 6. Modal constants extracted from 3 different sets of FRF

Mode	YY[a]	SY[b]	CS[c]
1st	10.397	7.253	13.027
2nd	35.538	0.143	36.926
3rd	65.150	21.200	65.799
4th	94.623	1.092	100.750
5th		31.200	
6th		1.090	
7th		65.310	

[a]FRF with both input and output in the y-direction.

[b]FRF with input in the S-direction and output in the y-direction.

[c]FRF compensated from the case SY.

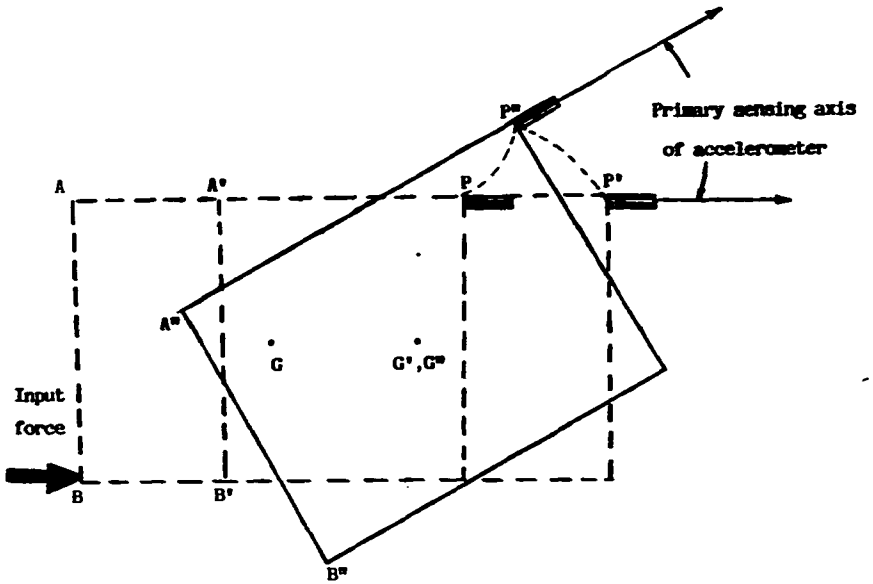

Fig. 1. Direction of primary sensing axis of accelerometer attached to a structure which undergoes general motion (translation + rotation).

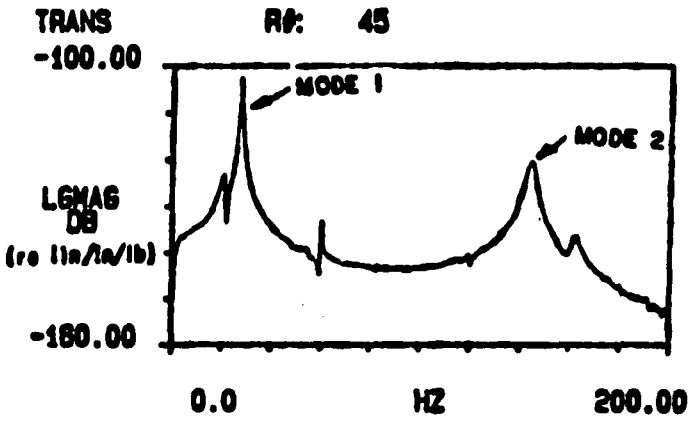

(a)

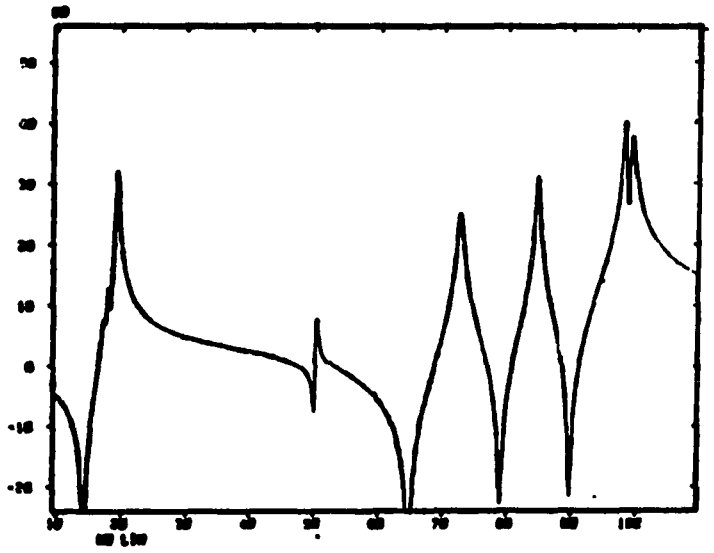

(b)

Fig. 2. Examples of frequency response functions used to extract modal parameters.

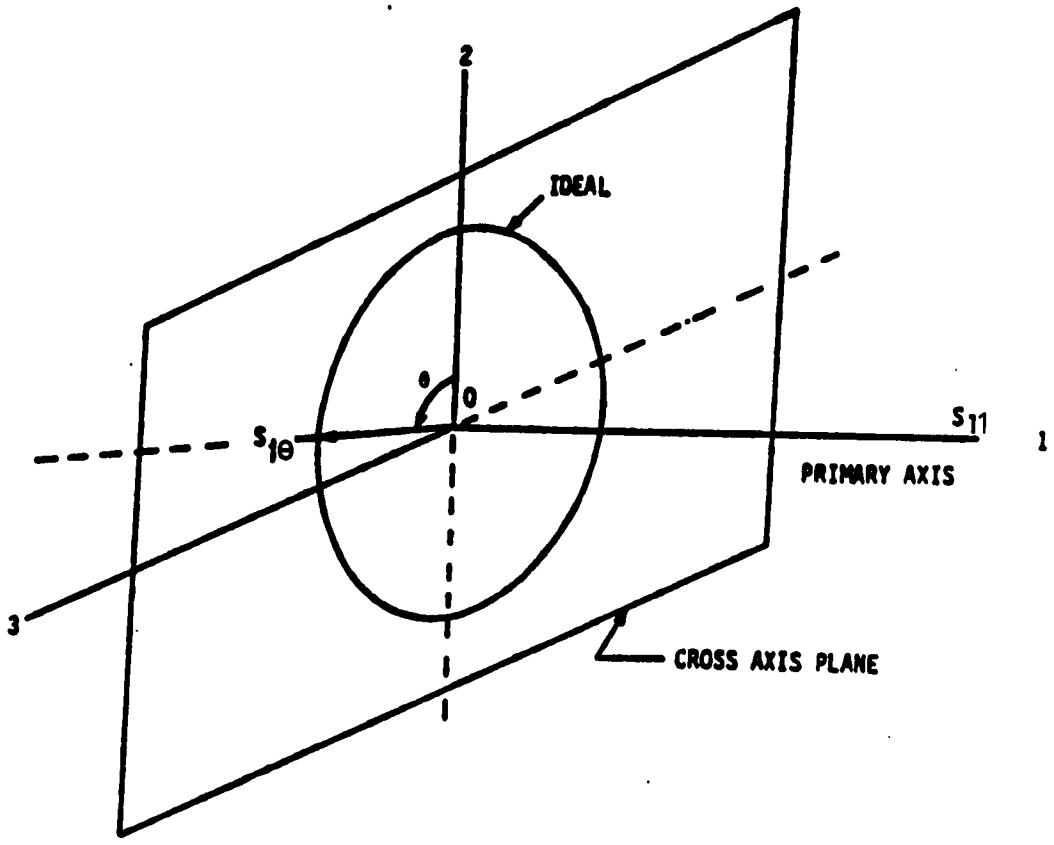

Fig. 3. Sketch showing primary sensing axis and cross-axis sensing plane.

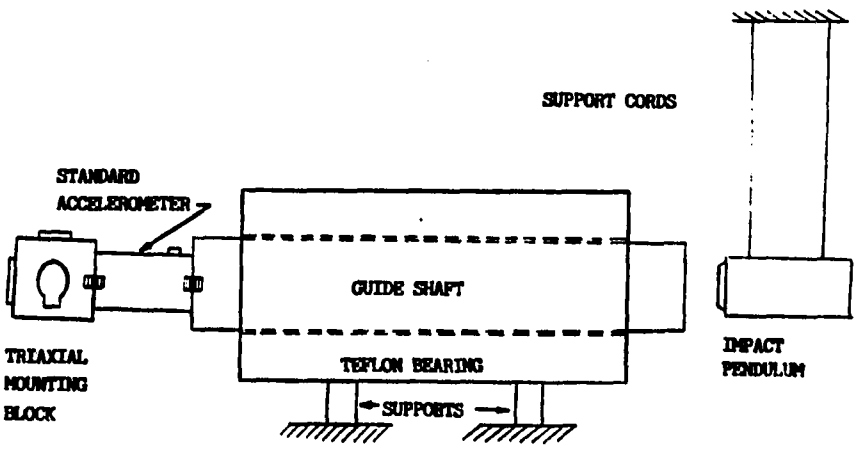

Fig. 4. Schematic diagram of triaxial accelerometer calibrator.

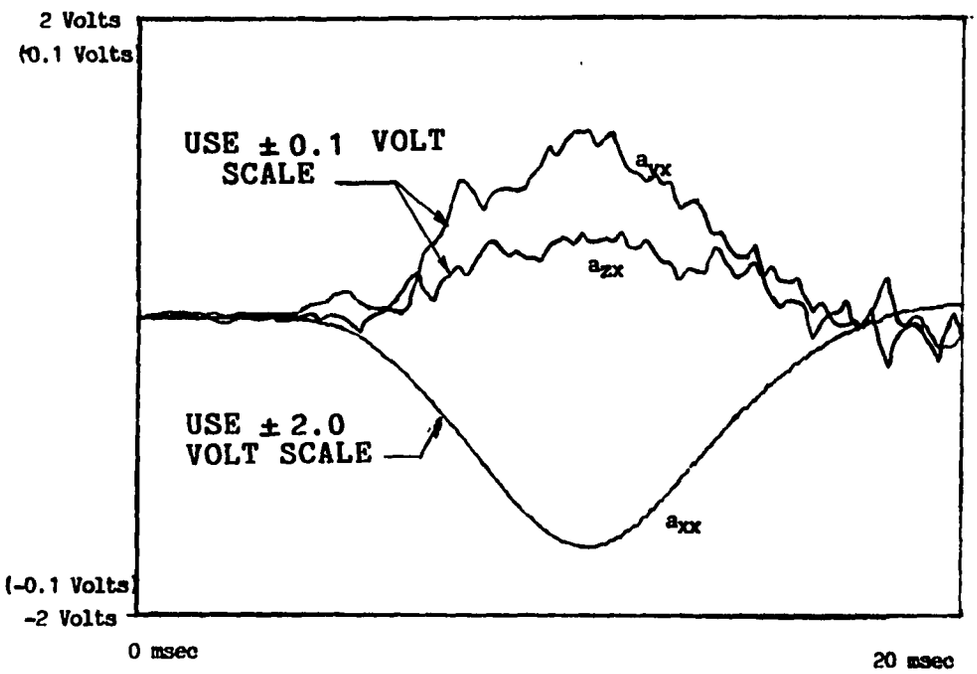

Fig. 5. Time history of impulse signal sensed by the triaxial accelerometer mounted on the calibrator with input impulse in the x-direction.
a_{xx}: signal from the accelerometer whose primary sensing axis is in the x-direction.
a_{yx}: signal from the accelerometer whose primary sensing axis is in the y-direction.
a_{zx}: signal from the accelerometer whose primary sensing axis is in the z-direction.

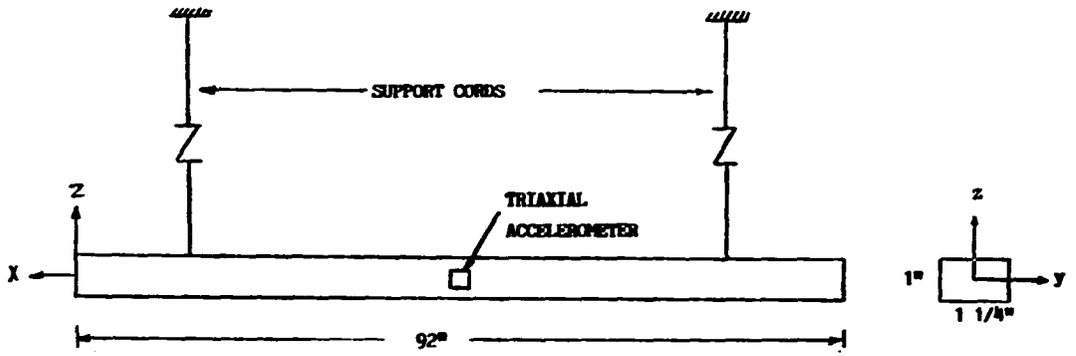

Fig. 6. Dimensions of the resonant bar showing coordinates and position of the triaxial accelerometer.

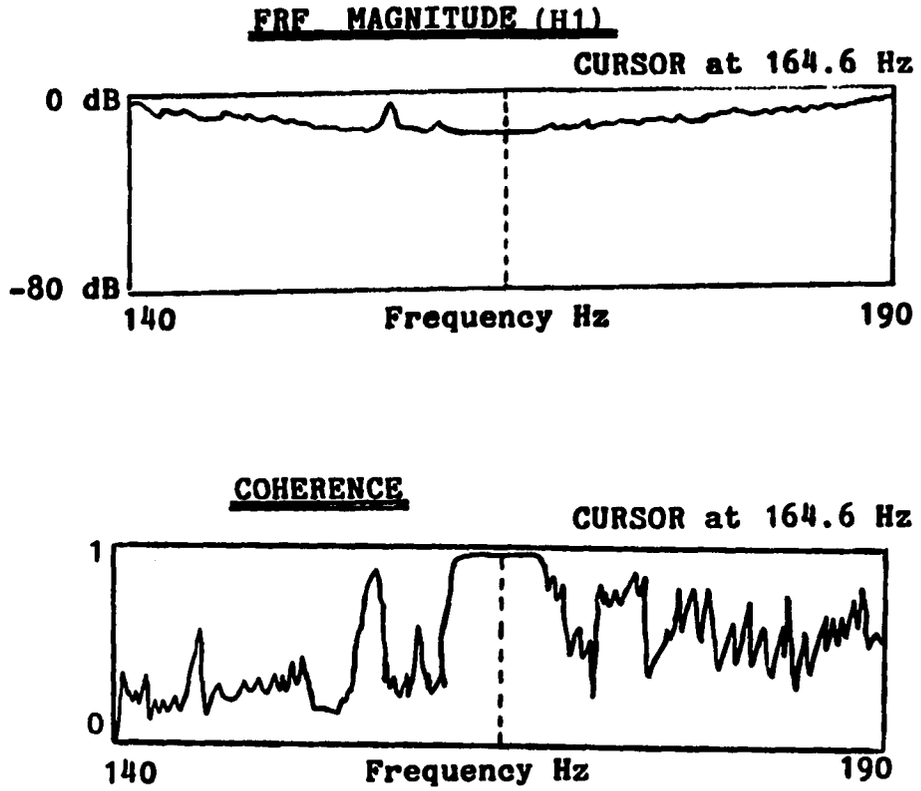

Fig. 7. Zoom measurement of FRF and coherence function between the standard accelerometer signal and cross-axis signal with the primary sensing axis in the x-direction around 3rd natural frequency of the resonant bar.

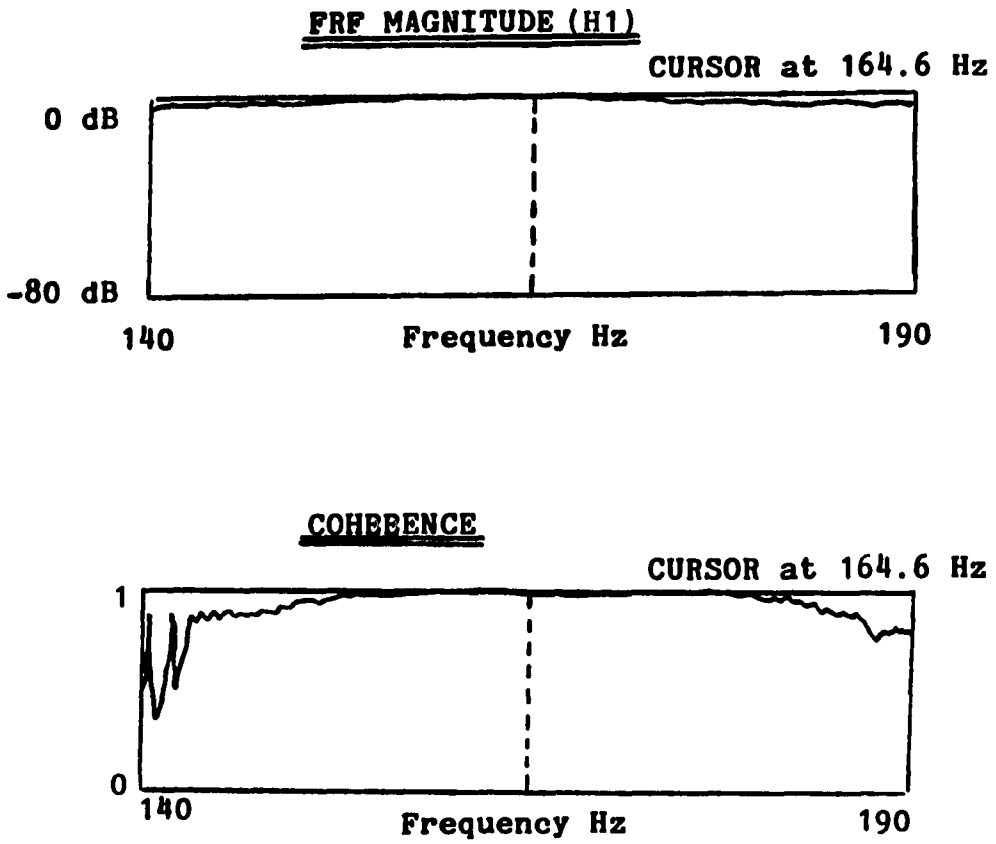

Fig. 8. Zoom measurement of FRF and coherence function between the standard accelerometer signal and primary sensing axis signal with the primary sensing axis in the y-direction around 3rd natural frequency of the resonant bar.

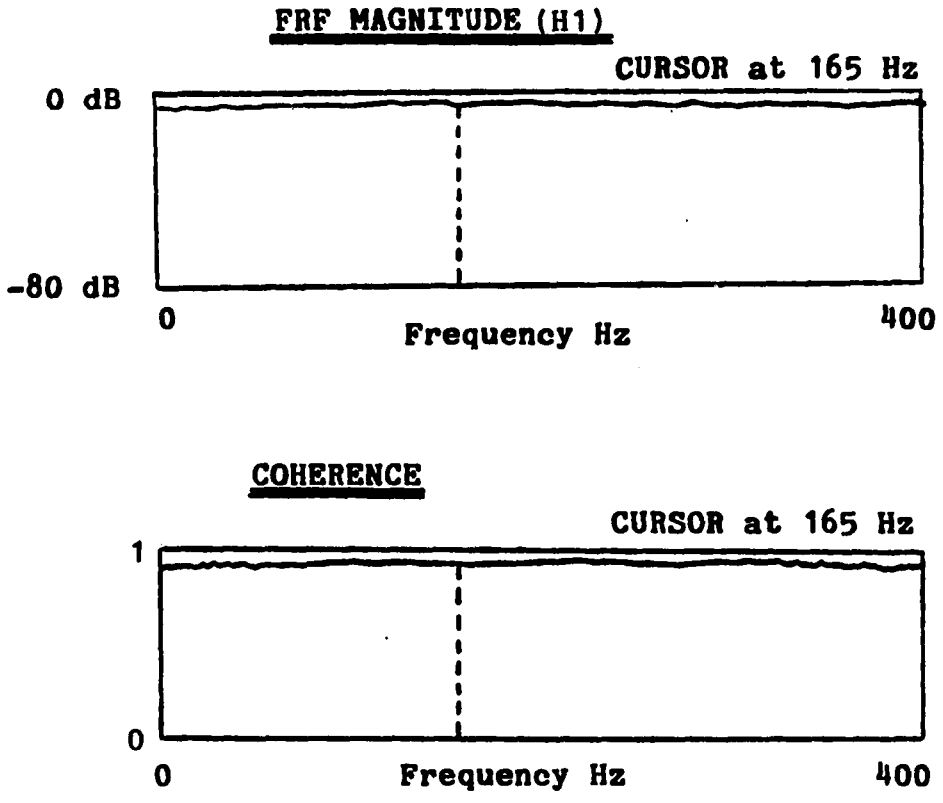

Fig. 9. Baseband measurement of FRF and coherence function between the standard accelerometer signal and primary sensing axis signal with the primary sensing axis in the y-direction up to 400 Hz.

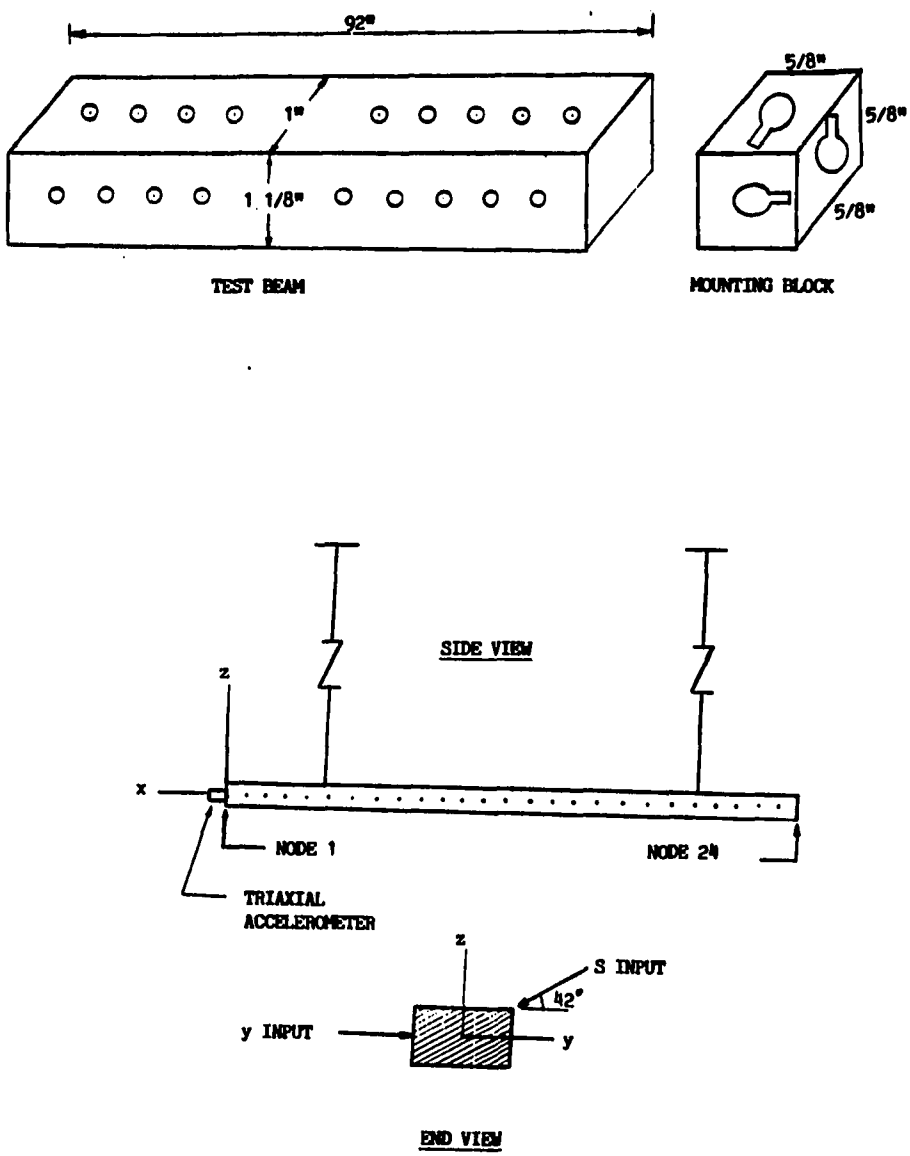

Fig. 10. Sketch of Free-Free beam showing coordinates and direction of impact.

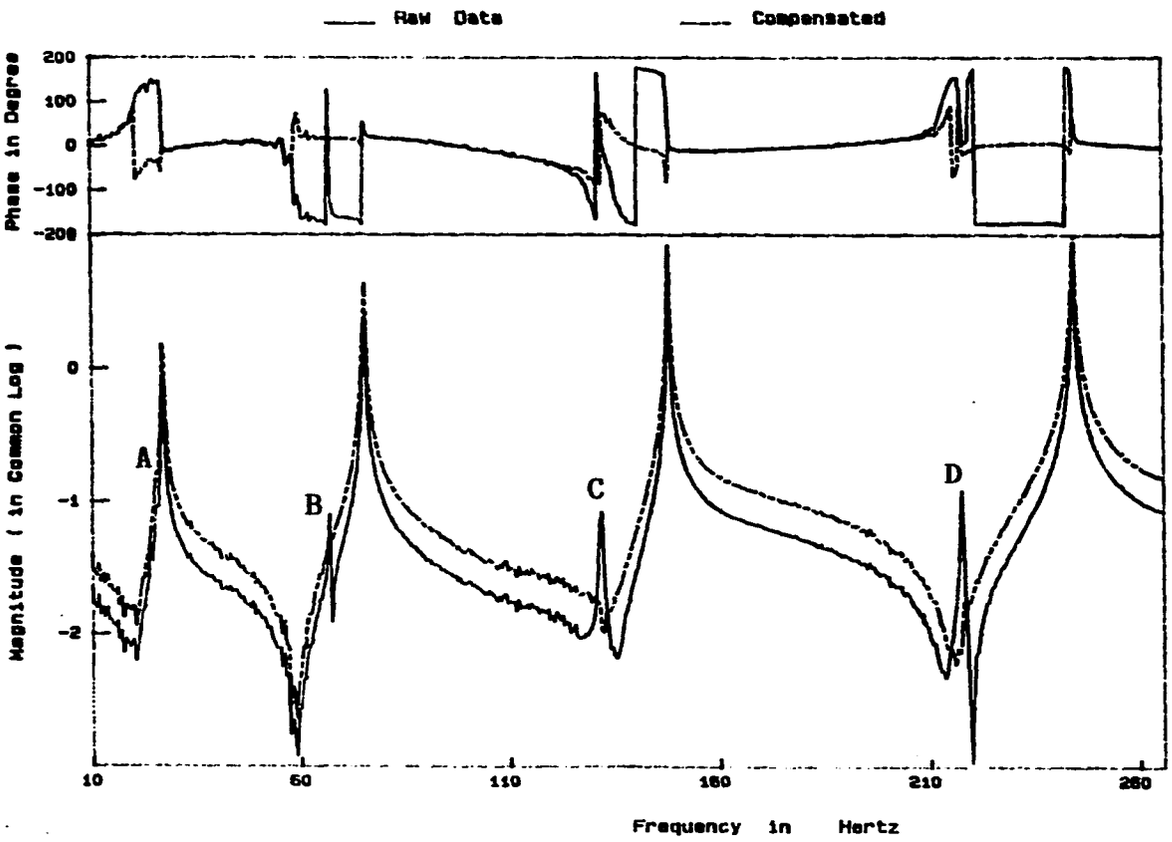

Fig. 11. Y-direction FRF at Node 1 for input in the S-direction with baseband measurement, and its compensated FRF.

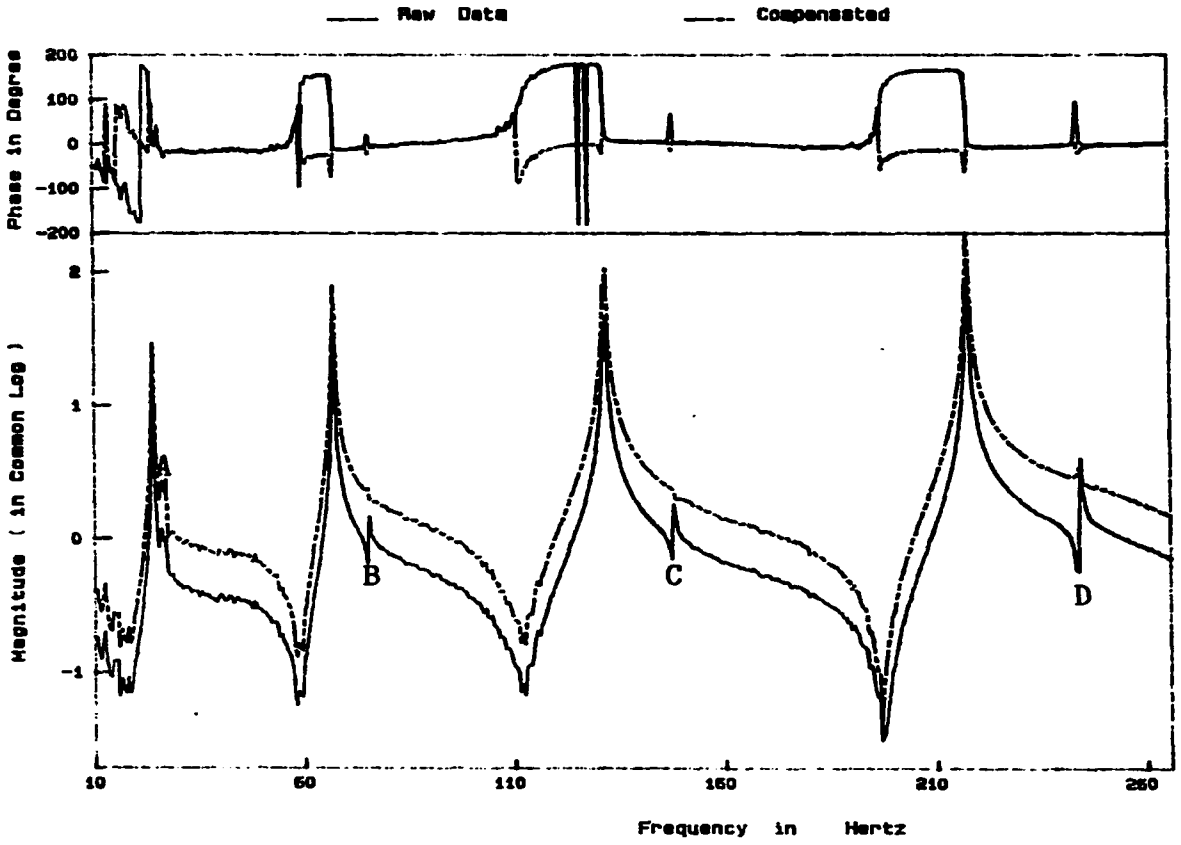

Fig. 12. Z-direction FRF at Node 1 for input in the S-direction with baseband measurement, and its compensated FRF.

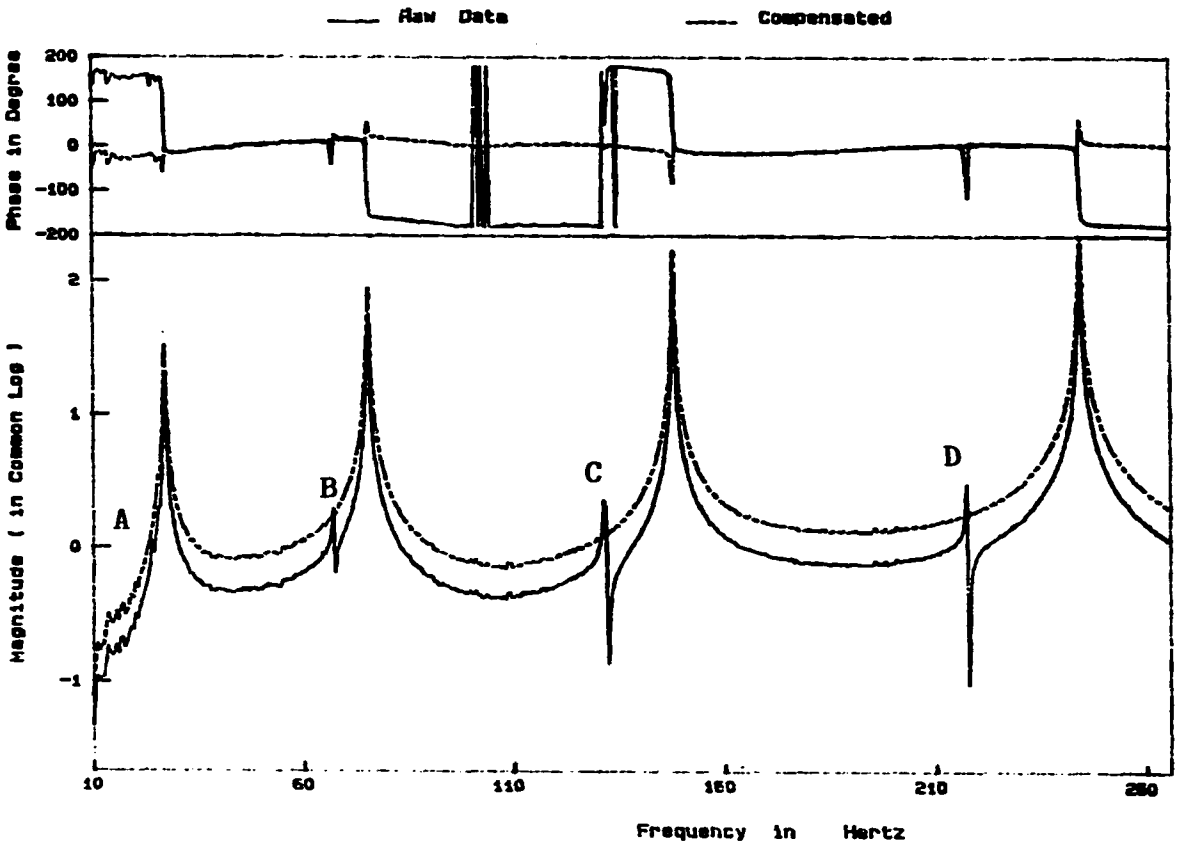

Fig. 13. Y-direction FRF at Node 24 for input in the S-direction with baseband measurement, and its compensated FRF.

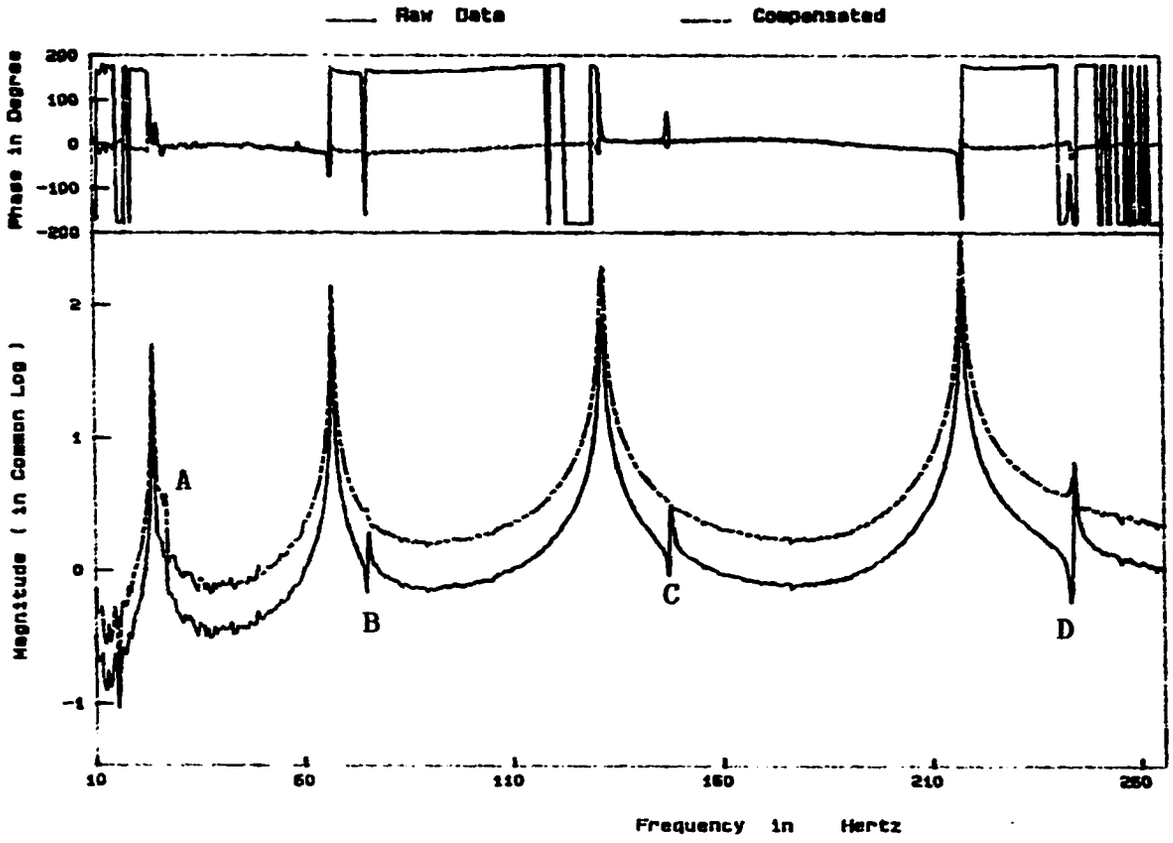

Fig. 14. Z-direction FRF at Node 24 for input in the S-direction with baseband measurement, and its compensated FRF.

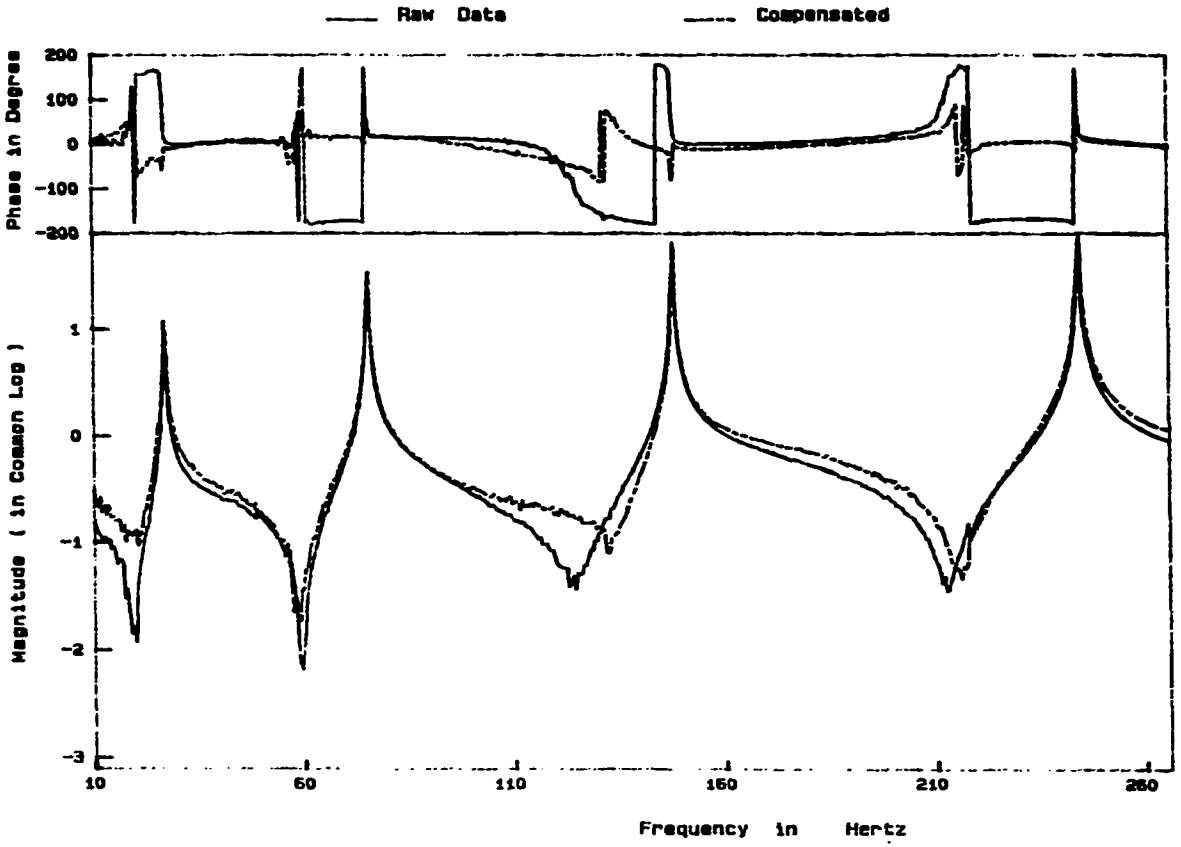

Fig. 15. Y-direction FRF at Node 1 for input in the y-direction with baseband measurement, and compensated FRF of Fig. 11.

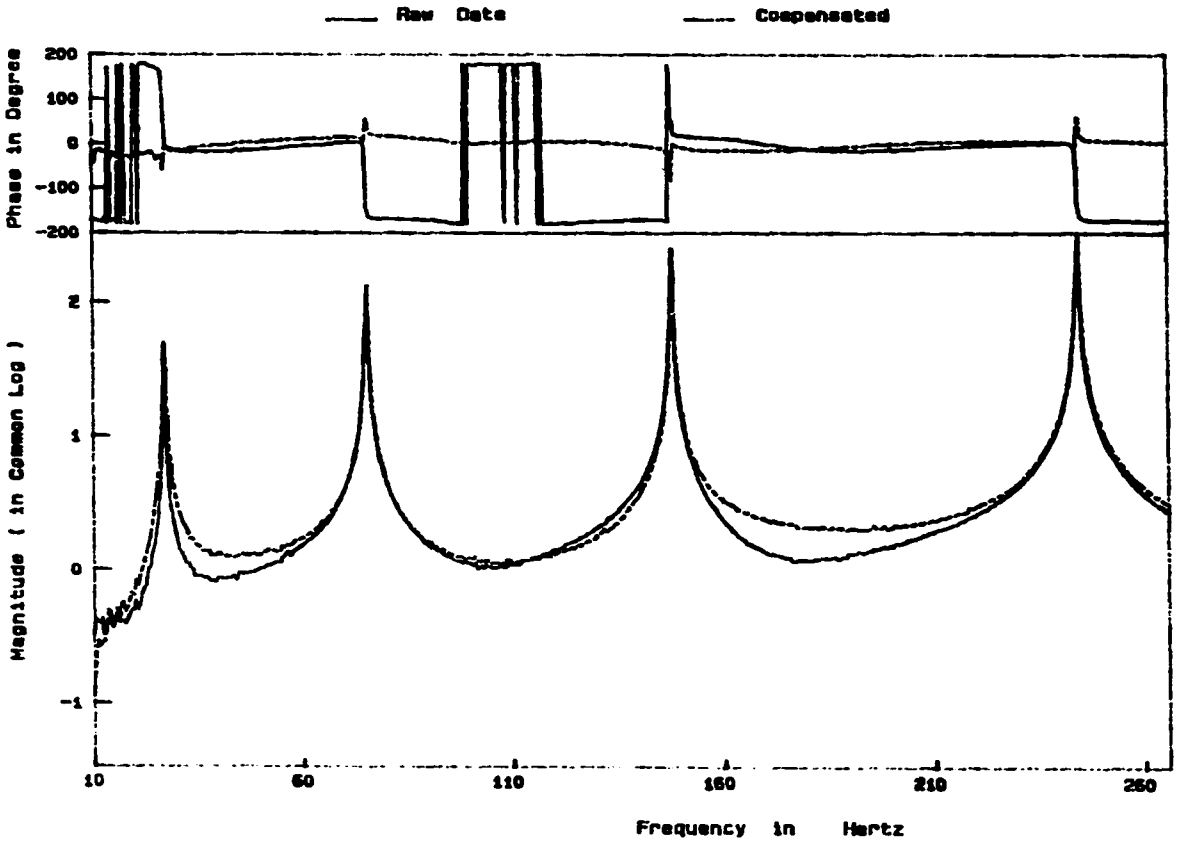

Fig. 16. Y-direction FRF at Node 24 for input in the y-direction with baseband measurement, and compensated FRF of Fig. 13.

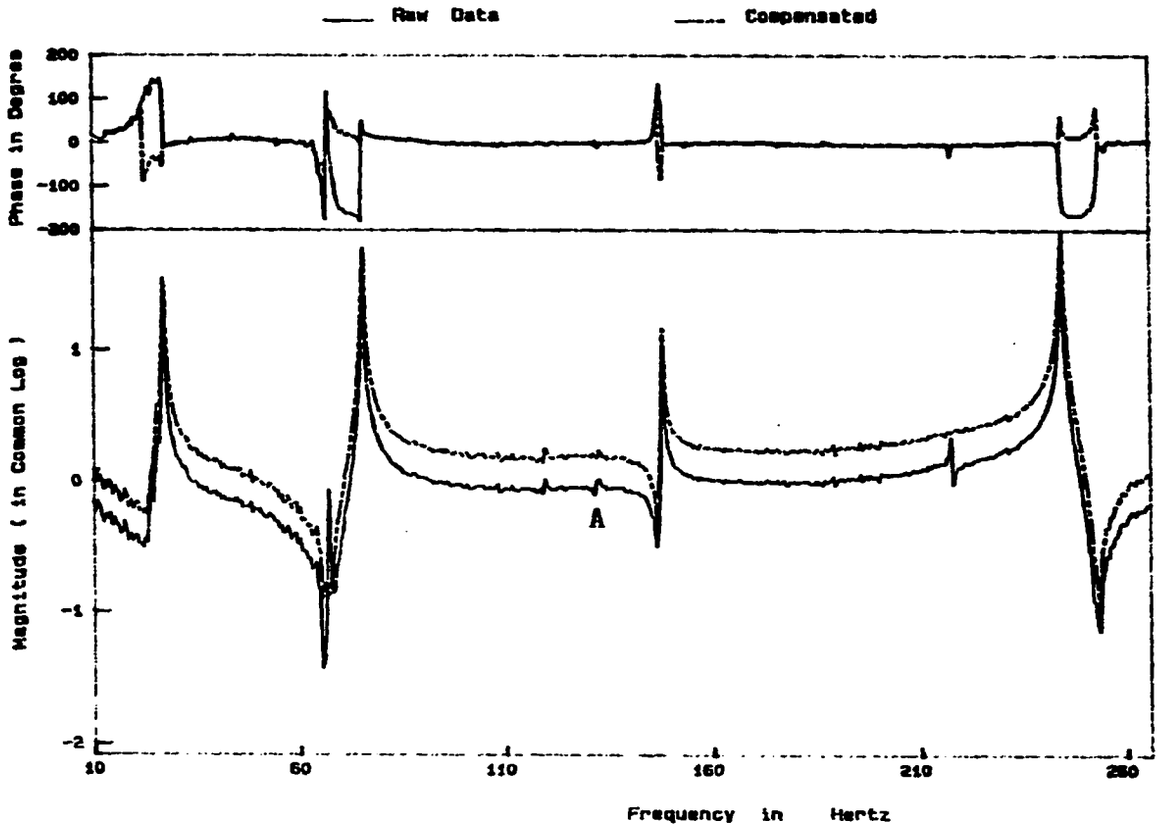

Fig. 17. Y-direction FRF at Node 3 for input in the S-direction with baseband measurement, and its compensated FRF.

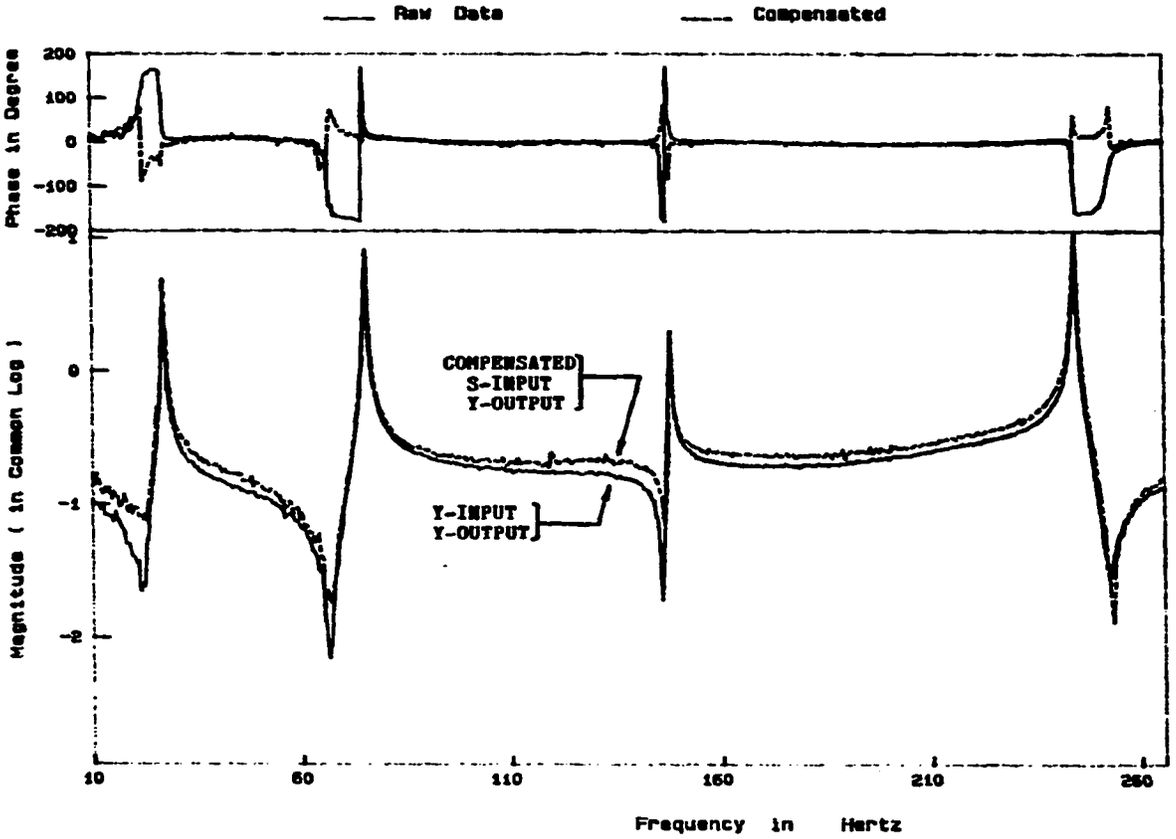

Fig. 18. Y-direction FRF at Node 3 for input in the y-direction with baseband measurement, and compensated FRF of Fig. 17.

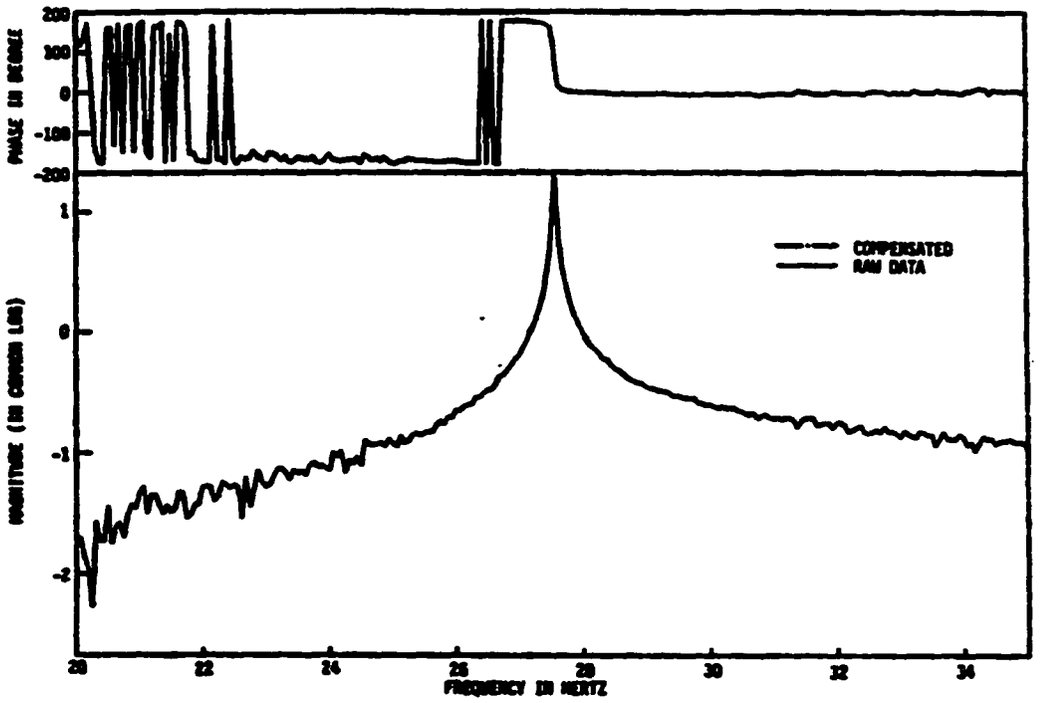

Fig. 19. Y-direction FRF for input in the y-direction with zoom measurement around the 1st mode, and its compensated FRF.

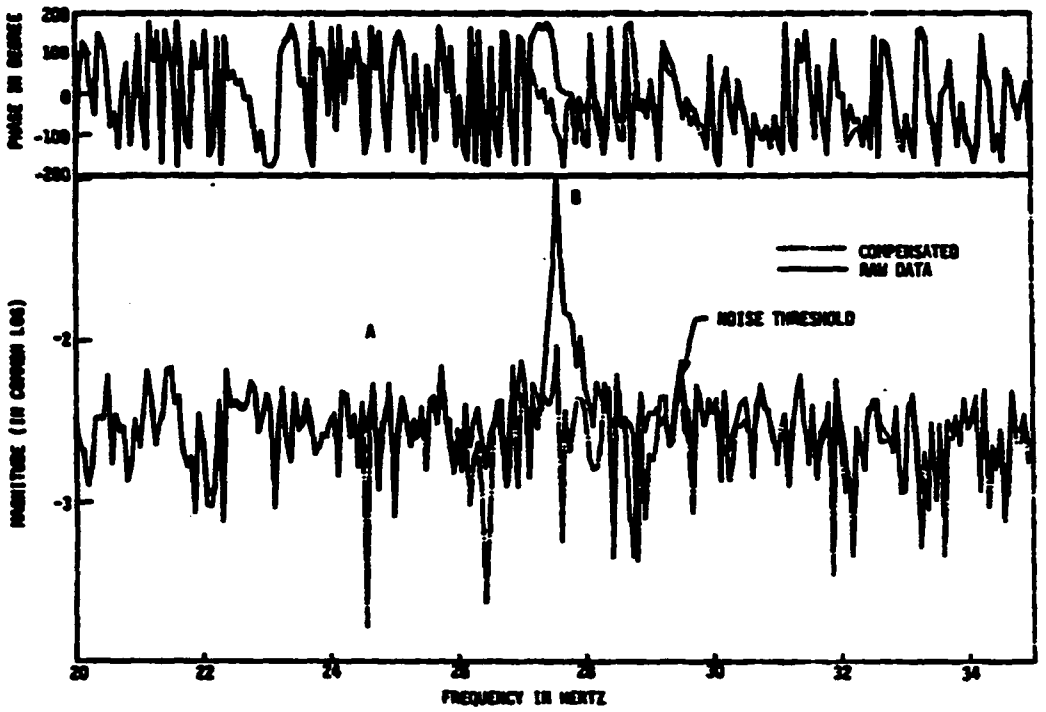

Fig. 20. X-direction FRF for input in the y-direction with zoom measurement around the 1st mode, and its compensated FRF.

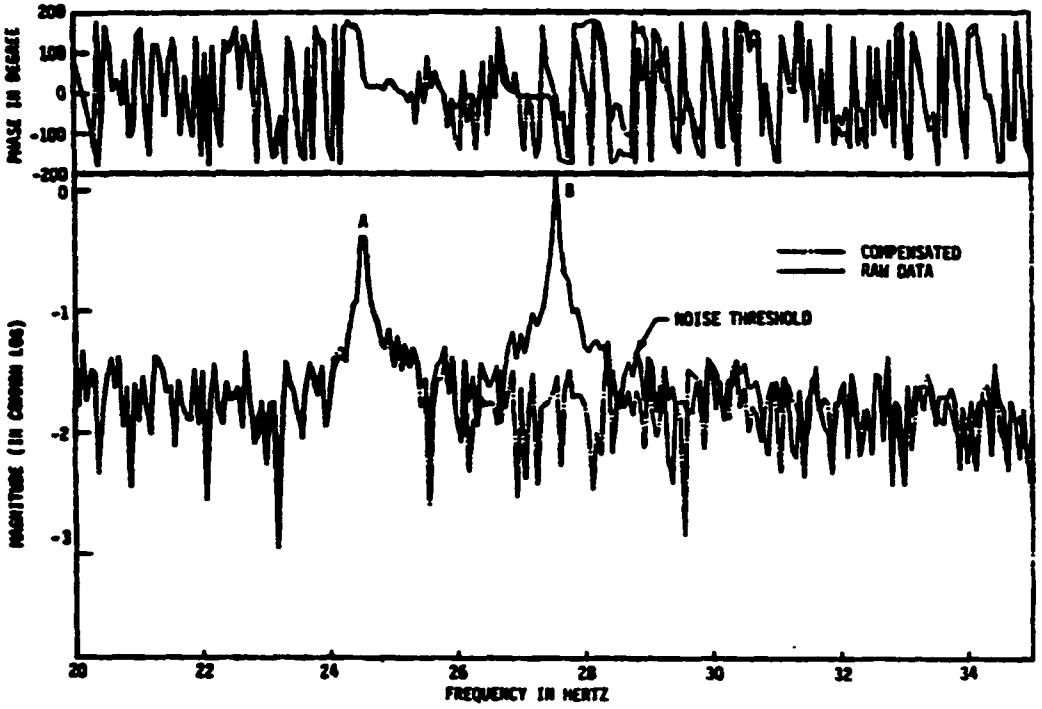

Fig. 21. Z-direction FRF for input in the y-direction with zoom measurement around the 1st mode, and its compensated FRF.

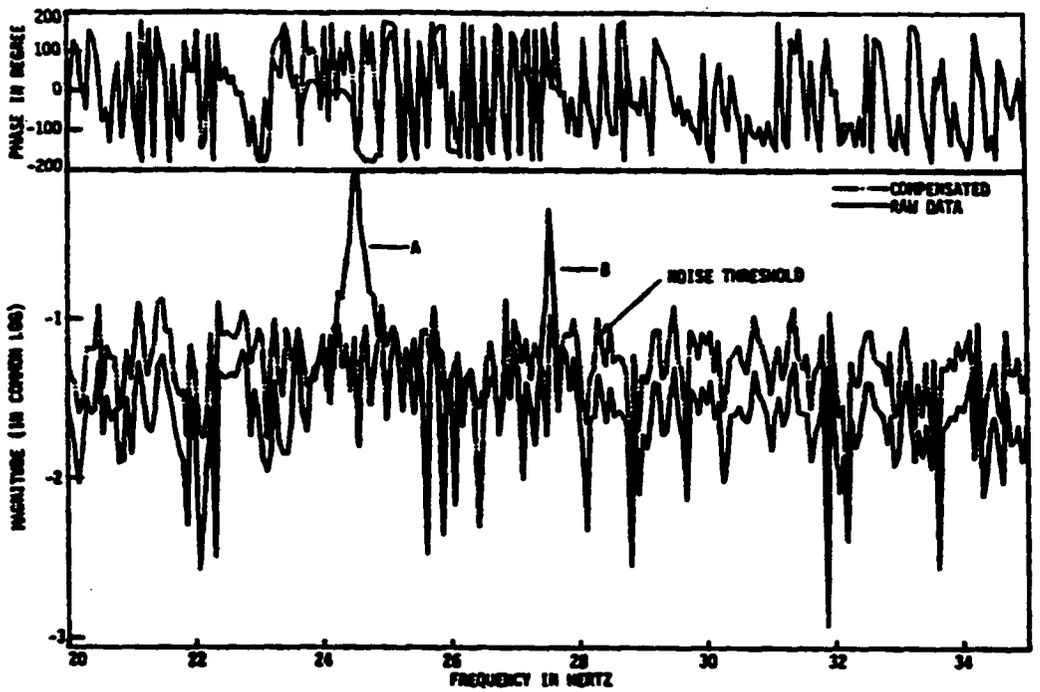

Fig. 22. X-direction FRF for input in the S-direction with zoom measurement around the 1st mode, and its compensated FRF.

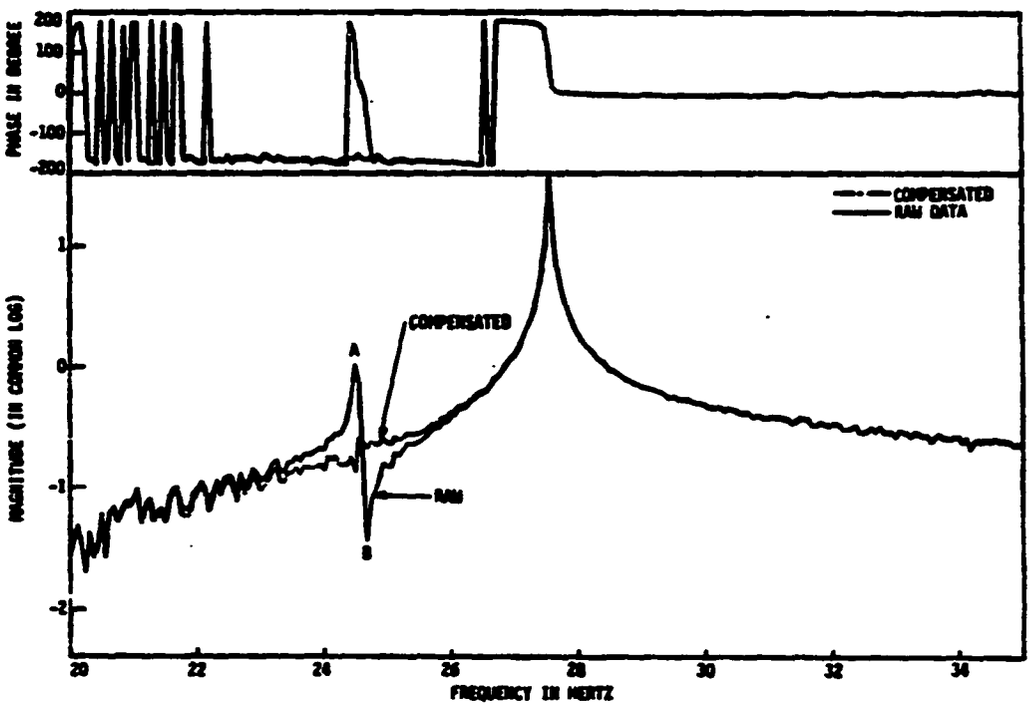

Fig. 23. Y-direction FRF for input in the S-direction with zoom measurement around the 1st mode, and its compensated FRF.

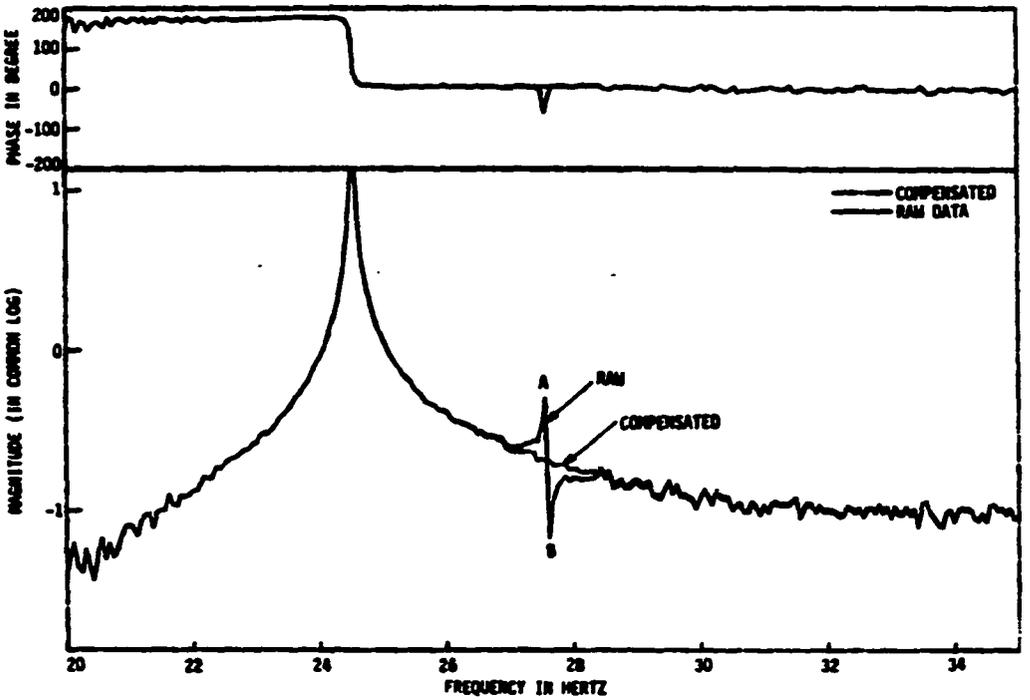

Fig. 24. Z-direction FRF for input in the S-direction with zoom measurement around the 1st mode, and its compensated FRF.

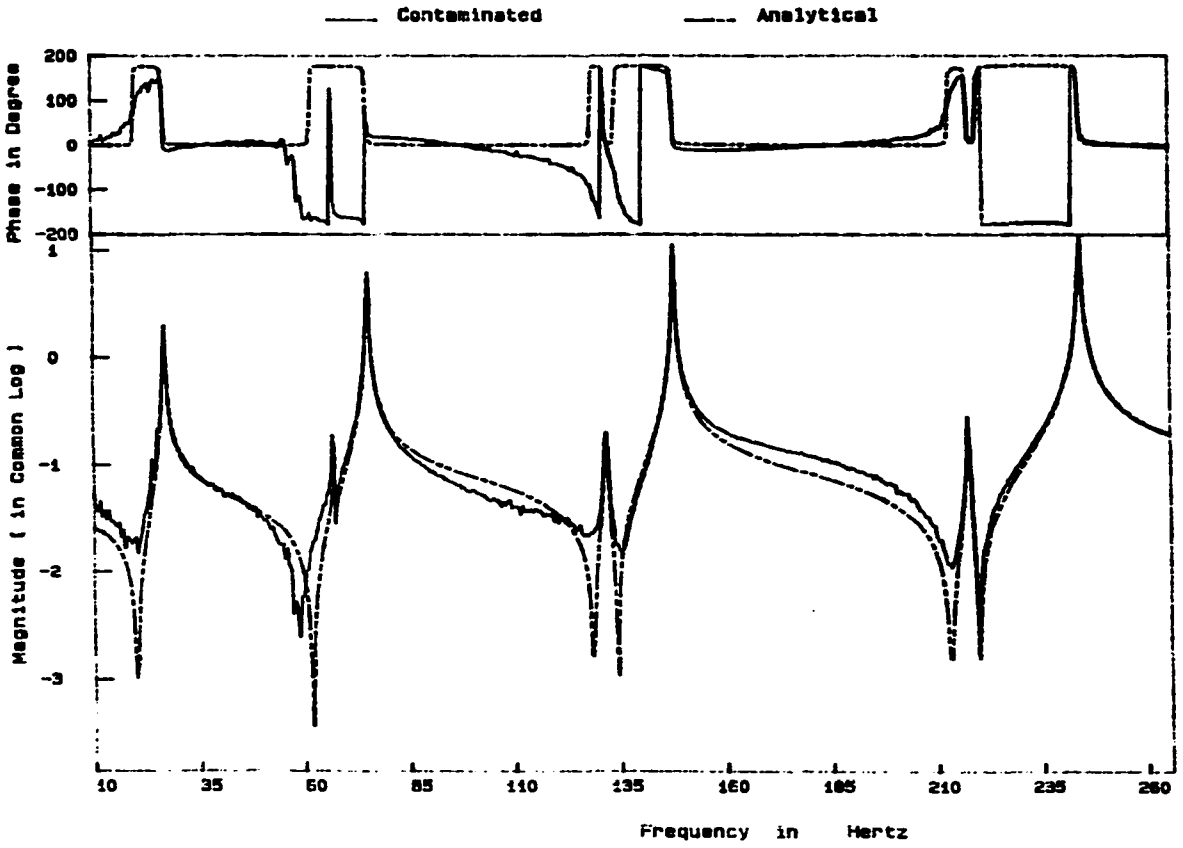

Fig. 25. Y-direction FRF for input in the S-direction with baseband measurement, and its equivalent analytical model generated by Modal-Plus.

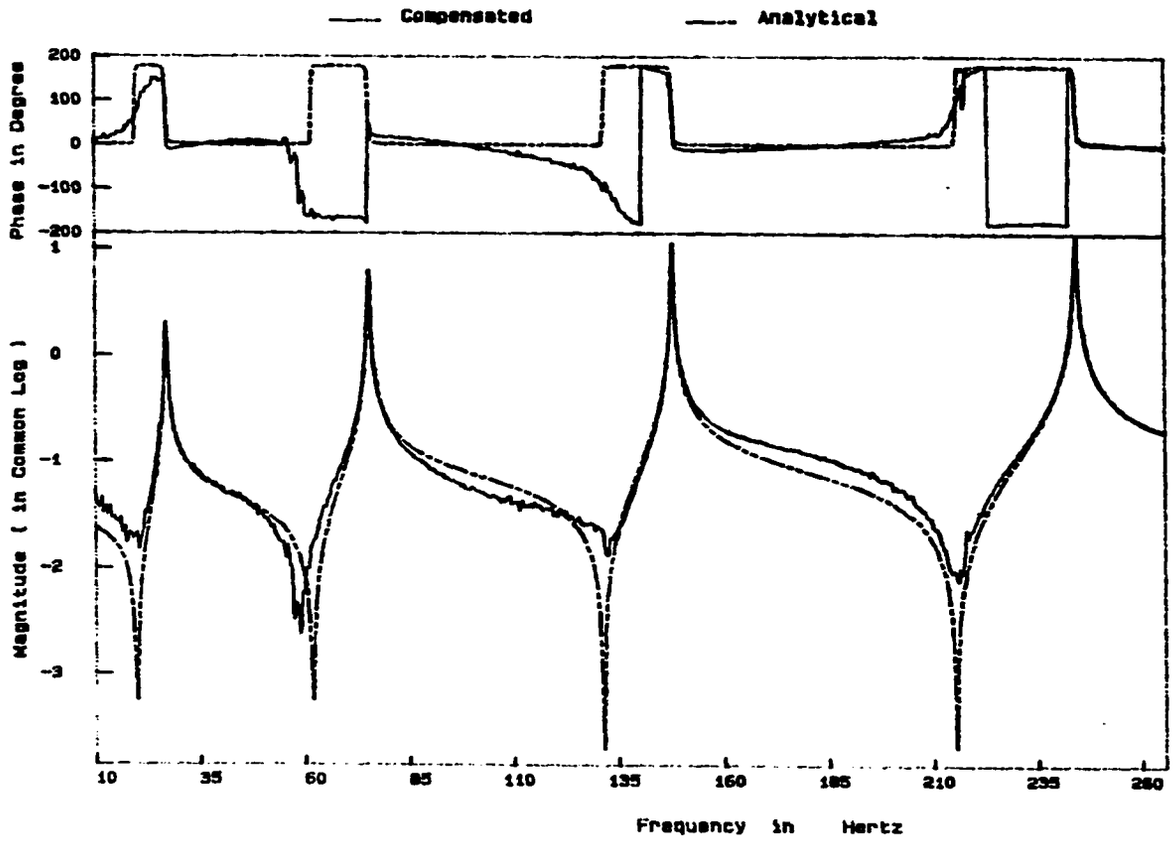

Fig. 26. Compensated y-direction FRF for input in the S-direction with baseband measurement, and its equivalent analytical model generated by Modal-Plus.

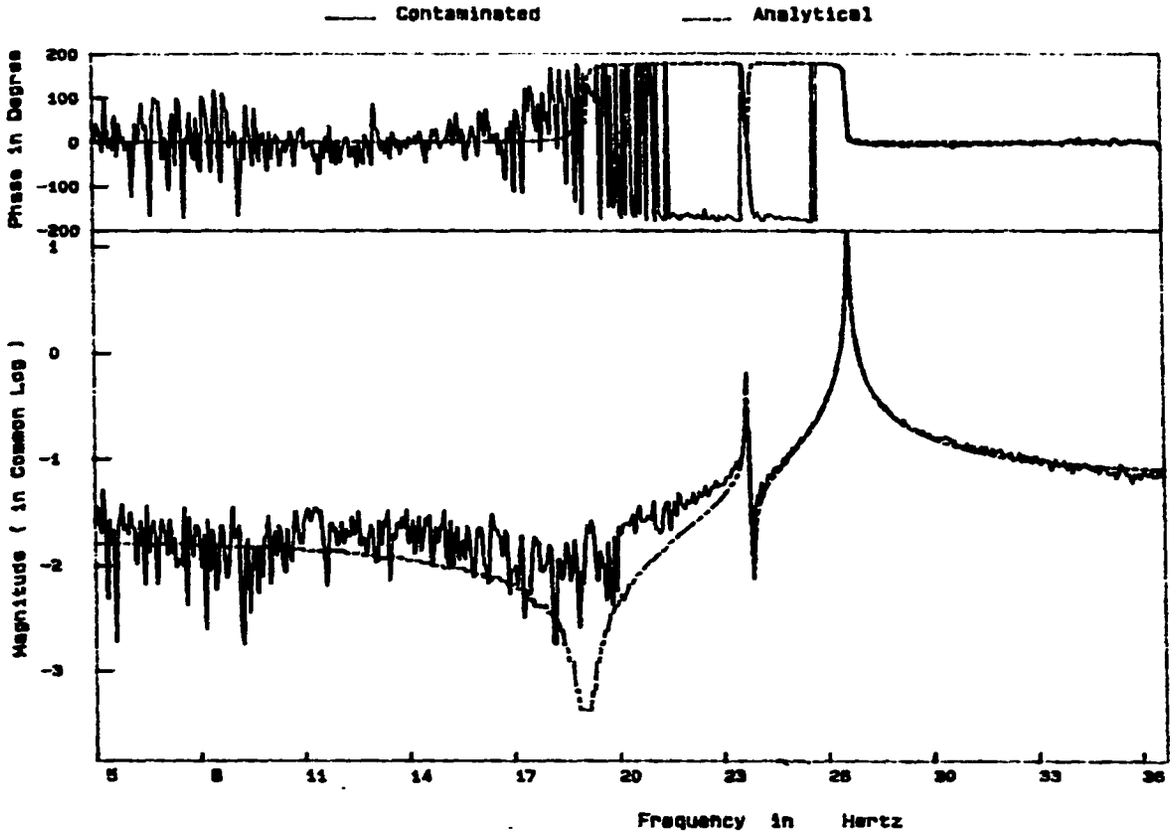

Fig. 27. Y-direction FRF for input in the S-direction with zoom measurement around the 1st mode, and its equivalent analytical model generated by Modal-Plus.

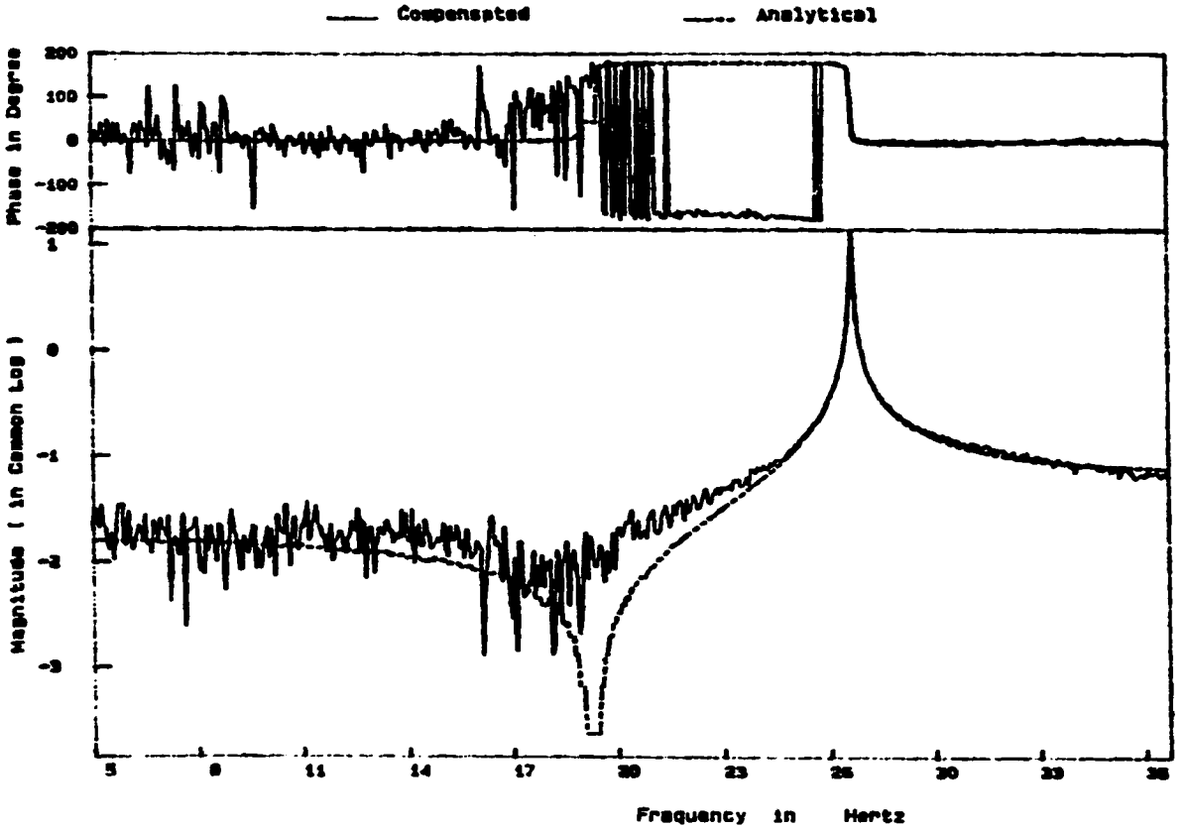

Fig. 28. Compensated y-direction FRF for input in the S-direction with zoom measurement, and its equivalent analytical model generated by Modal-Plus.

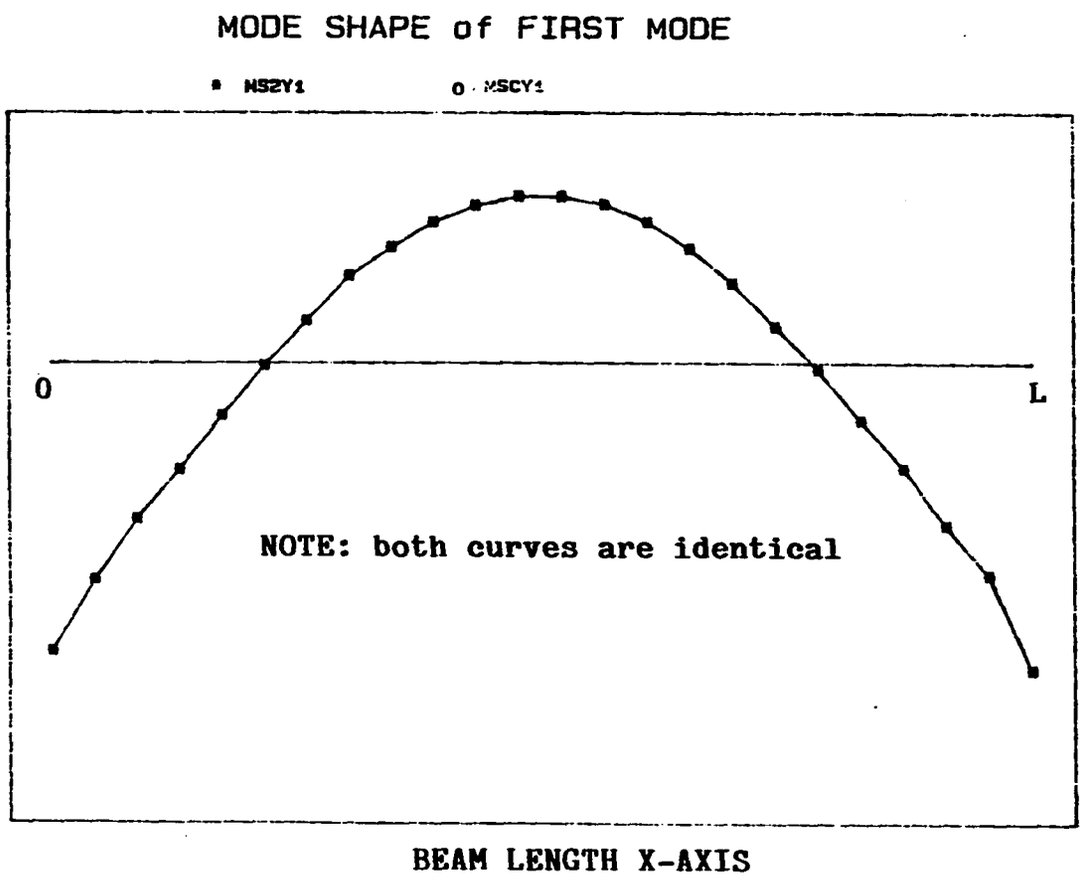

Fig. 29. 1st mode shape of the test beam in the y-direction.
* : 1st mode shape of the beam extracted from the raw FRFs.
o : 1st mode shape of the beam extracted from the compensated FRFs.

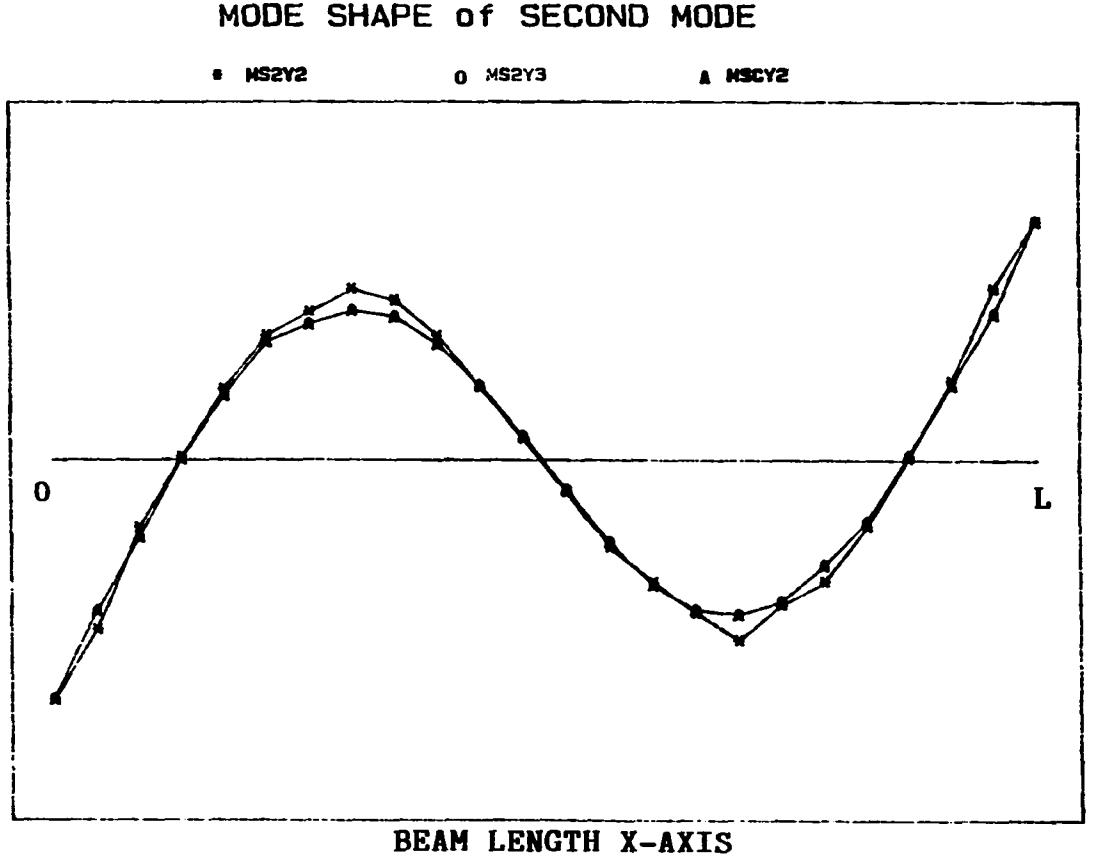

Fig. 30. 2nd mode shape of the test beam in the y-direction.
* : 2nd mode shape of the beam extracted from the raw FRFs.
o : 3rd mode shape of the beam extracted from the raw FRFs.
A : 2nd mode shape of the beam extracted from the compensated FRFs.

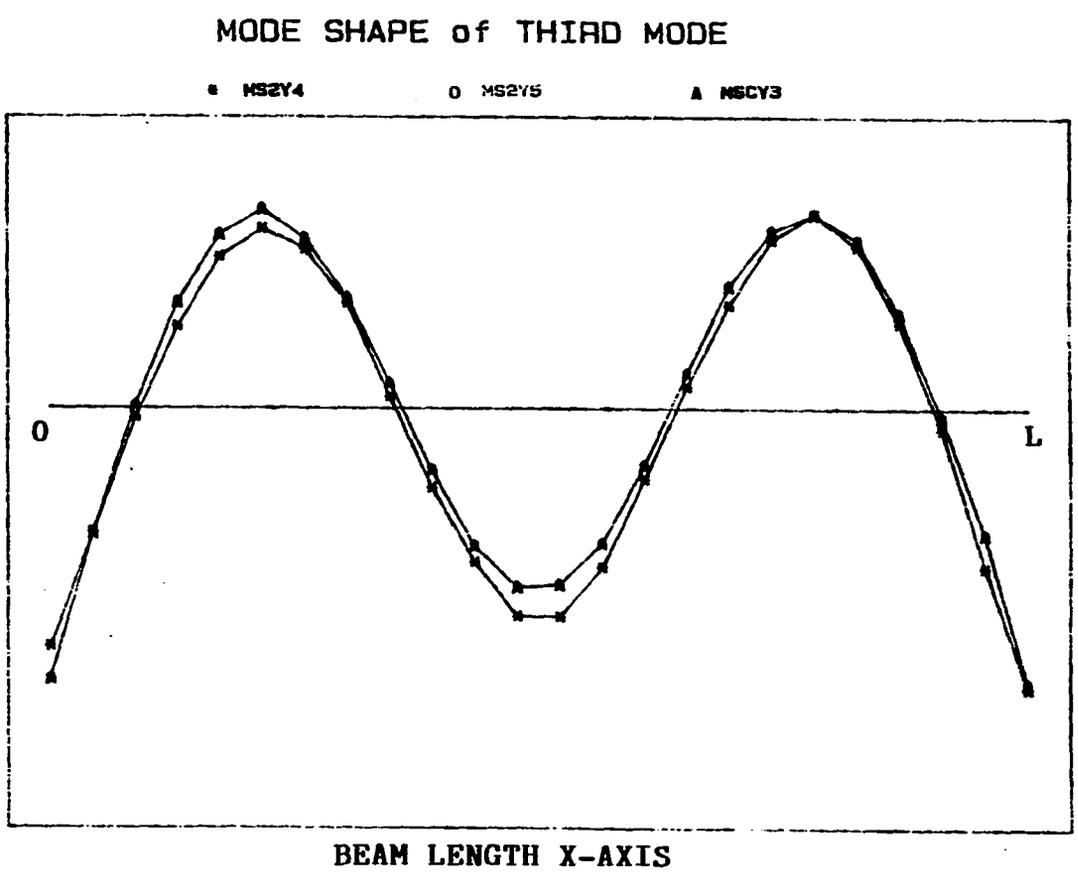

Fig. 31. 3rd mode shape of the test beam in the y-direction.
* : 4th mode shape of the beam extracted from the raw FRFs.
o : 5th mode shape of the beam extracted from the raw FRFs.
A : 3rd mode shape of the beam extracted from the compensated FRFs.

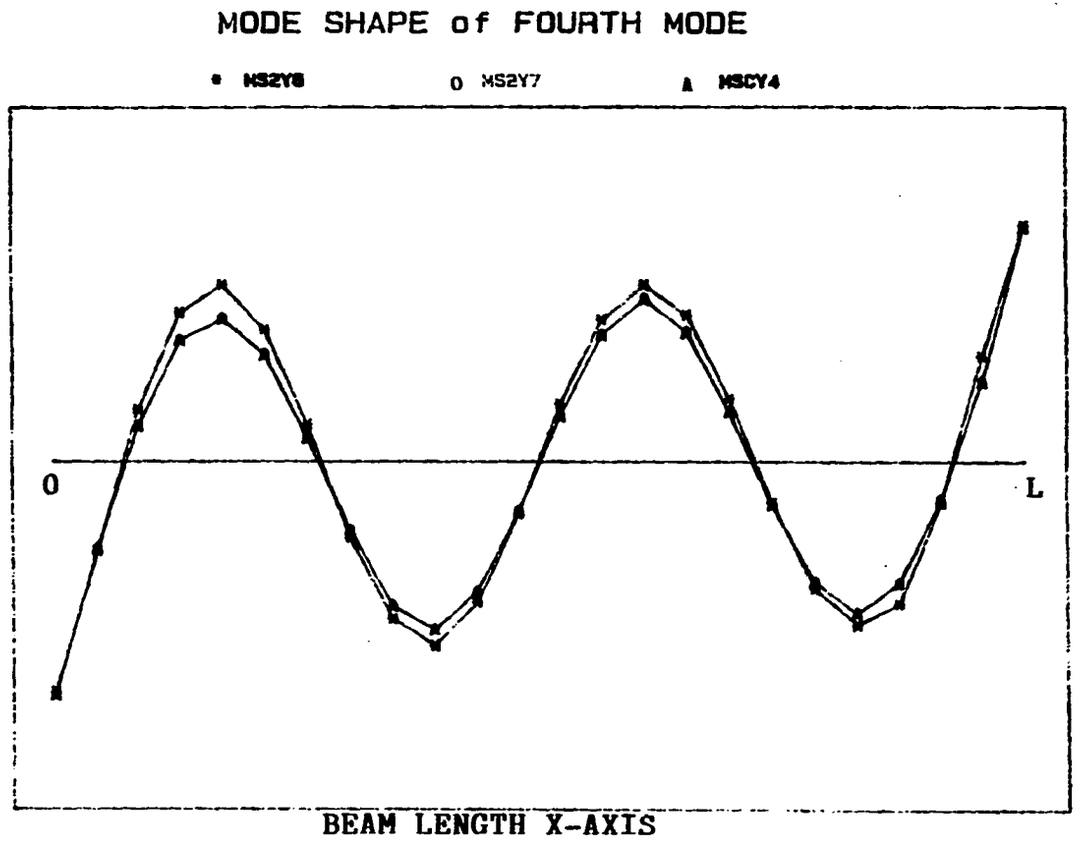

Fig. 32. 4th mode shape of the test beam in the y-direction.
* : 6th mode shape of the beam extracted from the rav FRFs.
o : 7th mode shape of the beam extracted from the rav FRFs.
A : 4th mode shape of the beam extracted from the compensated FRFs.

IX. APPENDIX A. BRIEF REVIEW OF THEORETICAL ASPECTS OF MODAL ANALYSIS

A. General

Modal analysis is a technique that is used to describe the dynamic responses of complex structures. It is based on the concept that each natural frequency has a unique shape of vibration called a mode shape. A large quantity of literature is rapidly developing, one concerned with theoretical modeling problems while the other is concerned with experimental methods of determining structural dynamic characteristics.

Structural vibration analysis usually starts by approximating a continuous system by a N degree of freedom system, where N is a finite number depending on the accuracy desired. For an N degree of freedom system, the behavior of the system can be expressed by the following equations of motion.

$$[M]\{x\} + [C]\{\dot{x}\} + [K]\{x\} = \{f\} \qquad \text{(A1)}$$

where $[M]$ = N X N mass matrix

$[C]$ = N X N damping matrix

$[K]$ = N X N stiffness matrix

$\{x\}$ = displacement time history vector

$\{\dot{x}\}$ = velocity time history vector

$\{\ddot{x}\}$ = acceleration time history vector

$\{f\}$ = excitation time history vector applied to the system

In the analytical approach, the analyst assigns reasonable values to the mass, damping, and stiffness of the system based on previous experience. Then, the homogeneous set of equations (A1) are solved in order to obtain the corresponding eigenvalues and eigenvectors for the system. The solution of the nonhomogeneous set of differential equations is assumed to be a superposition of the eigenvector multiplied by a time-dependent generalized coordinates. The procedure leads to an uncoupled set of differential equations in generalized coordinates, thus completing the solution [16].

On the other hand, the modal testing approach is based on the following equation.

$$H_{ij}(\omega) = \left(\frac{X_i}{F_j} \right) = \sum_{r=1}^{N} \frac{({}_r\phi_i)({}_r\phi_j)}{\lambda_r^2 - \omega^2} = \sum_{r=1}^{N} \frac{{}_rA_{ij}}{\lambda_r^2 - \omega^2} \qquad \text{(A2)}$$

where $H_{ij}(\omega)$ is frequency response function of system at position i due to input at j

X_i is Fourier transform of response at i

F_j is Fourier transform of input at j

λ_r^2 is the eigenvalue of the r^{th} mode (its natural frequency and damping factor combined)

${}_r\phi_i$ is the i^{th} element of the r^{th} eigenvector $\{\phi\}_r$ (namely, the relative displacement at that point during vibration in the r^{th} mode)

${}_rA_{ij}$ is the modal constant

(for mode r linking coordinate i and j)

N is the number of degrees of freedom

Equation (A2) suggests that the FRFs of the system can be described in terms of modal properties instead of spatial properties. The fact that FRFs are the quantities which can be measured in practice and, at the same time, can be expressed in terms of various mass, damping and stiffness elements of the system makes it possible to extract the mode of vibration directly from the measured FRFs without having to make any assumptions about the structural properties. This experimental approach ends up with a set of modes defined by frequency, damping, mode shape and modal constant.

B. Modal Parameter Extraction Methods

A major part of the modal parameter extraction procedure consists of curve-fitting a theoretical expression for an individual FRF to the actual measured FRF. Various different methods and corresponding algorithms are possible according to the type of FRF data and specific purpose of analysis. Each method has its own merits and drawbacks. Details of these methods and procedures are available throughout the current literature in this field, for example [1][17][18][19][20]. Thus, only a brief summary of few typical methods and their basic ideas are presented here.

1. Search peak method

This is the simplest, and thus, the traditional way to find out modal parameters directly from the magnitude of FRF without employing sophisticated numerical procedure.

First, the individual resonance peaks are detected on the FRF plot (Fig. A1), and the frequency of maximum response taken as the natural frequency ω_r of that mode.

Second, the maximum value of the FRF is noted (H^*) and the frequency bandwidth of the function for a response level of $H^*/\sqrt{2}$ is used to determined ($\Delta\omega = \omega_a - \omega_b$). The two points thus identified as ω_b and ω_a are called the 'half-power points' as shown in Fig. A1.

Third, the damping of the mode in question can now be estimated from one of the following formulae:

$$\eta_r = (\omega_a^2 - \omega_b^2)/\omega_r^2 \simeq \Delta\omega/\omega_r$$
$$\zeta_r = 2\eta_r \qquad \text{(A3)}$$

Where η_r is the damping loss factor for r^{th} mode.

Last, the modal constant of the mode being analyzed can be obtained by assuming that the total response in this resonant region is attributed to a single term in the general FRF series and calculated from the equation

$$H^* = A_r/(\omega_r^2 \eta_r)$$

or

$$A_r = H^* \omega_r^2 \eta_r \qquad (A4)$$

2. Circle fit method

This method is based on the fact that the Nyquist plot of typical FRF data produces a circle-like curve in the vicinity of resonance and assumes the behaviour of the system is dominated by the single mode being analyzed around that resonance.

Consider a receptance form of FRF with structural damping. Since the corresponding analysis applies equally well to other forms of the FRF with different types of damping, the particular case treated here is simply a matter of choice for convienience. For this case, Eq. (A2) can be rewritten as

$$H_{jk}(\omega) = \sum_{s=1}^{N} \frac{{}_sA_{jk}}{\omega_s^2 - \omega^2 + i\eta_s\omega_s^2} = \frac{{}_rA_{jk}}{\omega_r^2 - \omega^2 + i\eta_r\omega_r^2} + \sum_{\substack{s=1 \\ s\neq r}}^{N} \frac{{}_sA_{jk}}{\omega_s^2 - \omega^2 + i\eta_s\omega_s^2} \qquad (A5)$$

The single degree of freedom assumption is : for a small range of frequency in the vicinity of the natural frequency of the r^{th} mode, the second of the two terms in Eq. (A5) is approximately independent of frequency ω and the expression for the receptance may be written as

$$H_{jk}(\omega)_{\omega=\omega_r} = \frac{{}_rA_{jk}}{\omega_r^2 - \omega^2 + i\eta_r\omega_r^2} + {}_rB_{jk} \qquad (A6)$$

The basic function, which provides important properties of modal circle, is

$$\hat{H} = \frac{1}{\omega_r^2(1-(\omega/\omega_r)^2 + i\eta_r)} \qquad \text{(A7)}$$

Since the only effect of including the modal constant ${}_rA_{jk}$ and residual ${}_rB_{jk}$ is to scale, rotate and shift the modal circle about the origin, Eq. (A7) corresponds to the Nyquist plot shown in Fig. A2 and provides a means for extracting the required modal parameters. From Fig. A2, the r^{th} natural frequency (ω_r) can be easily located as the frequency at which the modal circle has a maximum imaginary (quadrature) value. The corresponding damping factor η_r is a reciprocal of diameter of modal circle. The actual scheme for estimating η_r is to choose two specific points on the circle, one corresponding to frequency (ω_b) below the natural frequency, and the other to one (ω_a) above the natural frequency as shown in Fig. A2. The following equations can be deduced from this figure.

$$\tan(\theta_b/2) = (1-(\omega_b/\omega_r)^2)/\eta_r$$
$$\tan(\theta_a/2) = ((\omega_a/\omega_r)^2-1)/\eta_r$$

thus,

$$\eta_r = (\omega_a^2-\omega_b^2)/\{\omega_r^2(\tan(\theta_a/2)+\tan(\theta_b/2))\} \qquad \text{(A8)}$$

Eq. (A8) is an exact expression, and applies for all levels of damping. If the system is lightly damped and two points for which $\theta_a=\theta_b=90^o$ (the half power points) are specified, the following familiar formula is obtained.

$$\eta_r = (\omega_2-\omega_1)/\omega_r \qquad \text{(A9)}$$

The final property related to the diameter of the circle which, for the quantity specified in Eq. (A7), is given by $1/\omega_r^2\eta_r$ provides the value of modal constant as follows;

$$|{}_rA_{jk}| = {}_rD_{jk}(\omega_r^2\eta_r) \tag{A10}$$

where ${}_rD_{jk}$ is diameter of modal circle in Fig. A2.

3. Complex exponential method

The expression for the receptance FRF of a general multi-degree of freedom system with viscous damping can be writen as

$$H_{jk}(\omega) = \frac{X_j}{F_k} = \sum_{r=1}^{N}\left(\frac{{}_rA_{jk}}{s-s_r} + \frac{{}_rA_{jk}^*}{s-s_r^*}\right) \tag{A11}$$

where ${}_rA_{jk}^*$ and s_r^* are the complex conjugates of ${}_rA_{jk}$ and s_r, respectively. The subscripts j and k are dropped for convenience while the complex conjugate term is considered to be independent. Then the frequency response function can be written simply as

$$H(\omega) = \sum_{r=1}^{2N}\frac{A_r}{s-s_r} \tag{A12}$$

where $A_{r+1} = A_r^*$

$S_{r+1} = s_r^*$

$r = 1,3,5,7, \cdots\cdots$

$s_r = -\zeta_r\omega_r + j\omega_r\sqrt{1-\zeta_r^2} \quad (j = \sqrt{-1})$

From classical theory, the corresponding Impulse Response Function (IRF) can be obtained by taking the inverse Fourier transform of the receptance to give

$$h(t) = \sum_{r=1}^{2N} A_r \exp(s_r t) \tag{A13}$$

If the original FRF has been measured at equally-spaced frequencies, the resulting IRF will be described at a corresponding number of equally-spaced time intervals ($\Delta t = 1/\Delta f$) and the value of h(t) for the Kth subinterval is

$$h(t) = \sum_{r=1}^{2N} A_r \exp(s_r K\Delta t) = \sum_{r=1}^{2N} A_r (U_r)^K \tag{A14}$$

where $K = 0,1,2, \cdots\cdots 2N$

Δt = value of the time subinterval

which, when extended to the full data set of q samples, gives

$$\begin{aligned}
h(t_0) &= A_1 + A_2 + \cdots\cdots\cdots\cdots + A_{2N} \\
h(t_1) &= A_1U_1 + A_2U_2 + \cdots\cdots\cdots\cdots + A_{2N}U_{2N} \\
h(t_3) &= A_1U_1^2 + A_2U_2^2 + \cdots\cdots\cdots\cdots + A_{2N}U_{2N}^2 \\
&\cdots \quad \cdots \quad \cdots \quad \cdots \\
h(t_q) &= A_1U_1^q + A_2U_2^q + \cdots\cdots\cdots\cdots + A_{2N}U_{2N}^q
\end{aligned} \tag{A15}$$

If 2N=q, there are q+1 rows for Eq. (A15). There must exist a polynomial of order q that satisfies the expression

$$U^q + \beta_1 U^{q-1} + \beta_2 U^{q-2} + \cdots\cdots + \beta_{q-1} U + \beta_q = 0 \qquad \text{(A16)}$$

whose roots are U_1, U_2, ... U_q. Therefore, the polynomial may also be written as

$$(U-U_1)(U-U_2)\cdots\cdots(U-U_q) = 0 \qquad \text{(A17)}$$

In order to determine the coefficients β_i of Eq. (A16), multiply row 1 of Eq. (A15) by β_q, the second row by β_{q-1}, etc., the qth row by q_1 and finally the q+1 row by β_0 (note β_0=1). Thus Eq. (A15) becomes

$$\begin{aligned}
\beta_q h(t_0) &= \beta_q (A_1 + A_2 + \cdots\cdots\cdots\cdots + A_{2N}) \\
\beta_{q-1} h(t_1) &= \beta_{q-1} (A_1 U_1 + A_2 U_2 + \cdots\cdots\cdots\cdots + A_{2N} U_{2N}) \\
&\cdots \\
\beta_1 h(t_{q-1}) &= \beta_1 (A_1 U_1^{q-1} + A_2 U_2^{q-1} + \cdots\cdots\cdots + A_{2N} U_{2N}^{q-1}) \\
\beta_0 h(t_q) &= \beta_0 (A_1 U_1^{q} + A_2 U_2^{q} + \cdots\cdots\cdots + A_{2N} U_{2N}^{q})
\end{aligned} \qquad \text{(A18)}$$

Summing all terms in Eq. (A18) yields,

$$\sum_{K=0}^{q} \beta_{q-K} h(t_K) = \sum_{K=0}^{q} \beta_{q-K} \left(\sum_{r=1}^{2N} A_r U_r^K \right) = \sum_{r=1}^{2N} A_r \left(\sum_{K=0}^{q} \beta_{q-K} U_r^K \right) \qquad \text{(A19)}$$

From Eq. (A16), the quantity

$$\sum_{K=0}^{q} \beta_{q-K} U_r^K = 0$$

since U_r is a root of this polynomial. Thus

$$\sum_{K=0}^{q} \beta_{q-K} h(t_K) = 0 \ , \quad \beta_0 = 1 \tag{A20}$$

An additional q-1 equations can be obtained by performing the same operation starting with the second row of Eq. (A15) and so on. An additional row must be added to Eq. (A15) for each additional equation thus obtained. The physical significance of these operations is to increase t_0 and t_q by Δt and therefore make the final sum invariant. The result is

$$\begin{bmatrix} h(t_{q-1}) & h(t_{q-2}) & \cdots\cdots & h(t_0) \\ h(t_q) & h(t_{q-1}) & \cdots\cdots & h(t_1) \\ \cdot & \cdot & & \cdot \\ h(t_{2q-2}) & h(t_{2q-3}) & \cdots\cdots & h(t_{q-1}) \end{bmatrix} \begin{Bmatrix} \beta_1 \\ \beta_2 \\ \cdot \\ \beta_q \end{Bmatrix} = \begin{Bmatrix} h(t_q) \\ h(t_{q+1}) \\ \cdot \\ h(t_{2q-1}) \end{Bmatrix} \tag{A21}$$

The above equation can be solved for the β's which may then be substituted into Eq. (A16) and the values of U_r are determined using an iterative polynomial solver. Values for ω_r and ζ_r can be found from the relationship in Eq. (A14). Finally, q rows of Eq. (A15) can be used to determine the modal constants A_1 through A_{2N} as follows

$$\begin{bmatrix} 1 & 1 & \cdots\cdots & 1 \\ U_1 & U_2 & \cdots\cdots & U_{2N} \\ U_1^2 & U_2^2 & \cdots\cdots & U_{2N}^2 \\ \cdot & \cdot & & \cdot \\ U_1^{2N-1} & U_2^{2N-1} & \cdots & U_{2N}^{2N-1} \end{bmatrix} \begin{Bmatrix} A_1 \\ A_2 \\ A_3 \\ \cdot \\ A_{2N} \end{Bmatrix} = \begin{Bmatrix} h(t_0) \\ h(t_1) \\ h(t_2) \\ \cdot \\ h(t_{2N-1}) \end{Bmatrix} \qquad \text{(A22)}$$

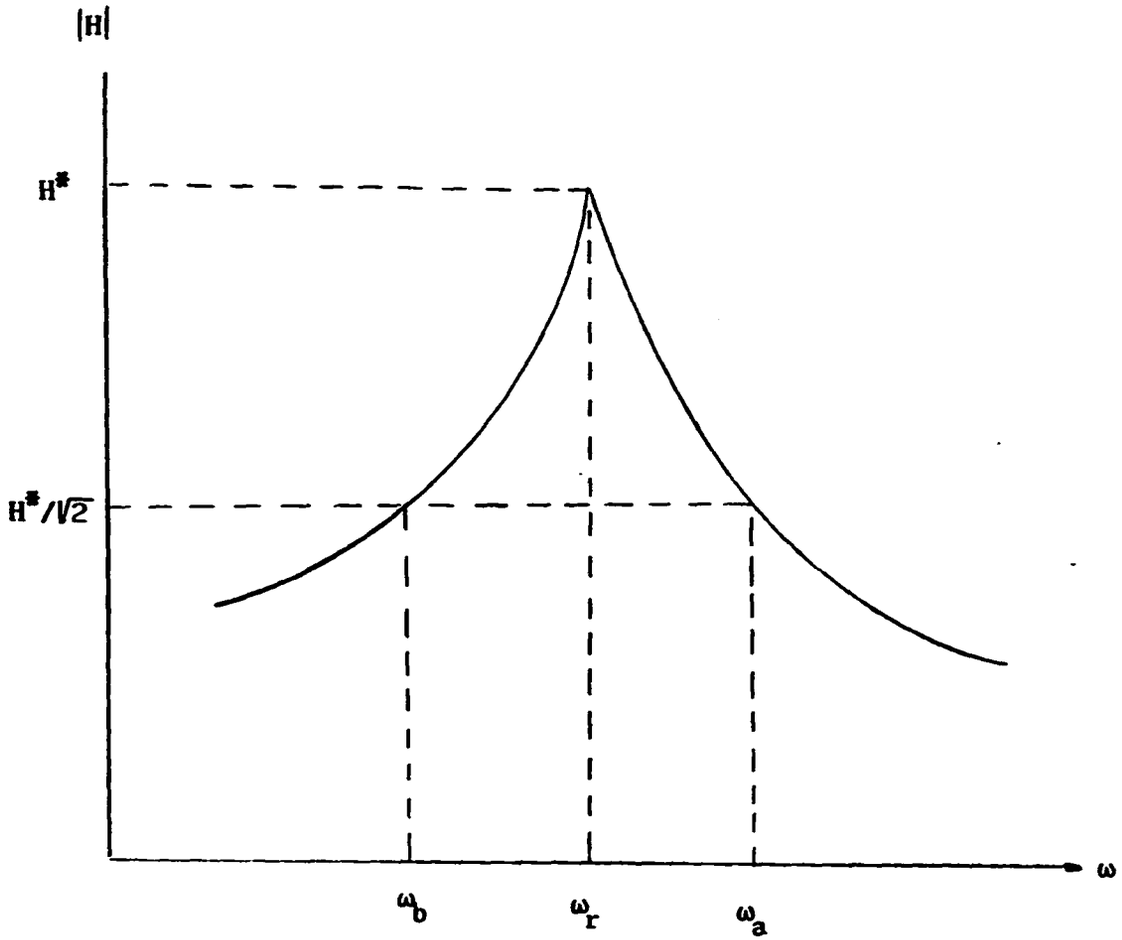

Fig. A.1. Details of magnitude of FRF around natural frequency.

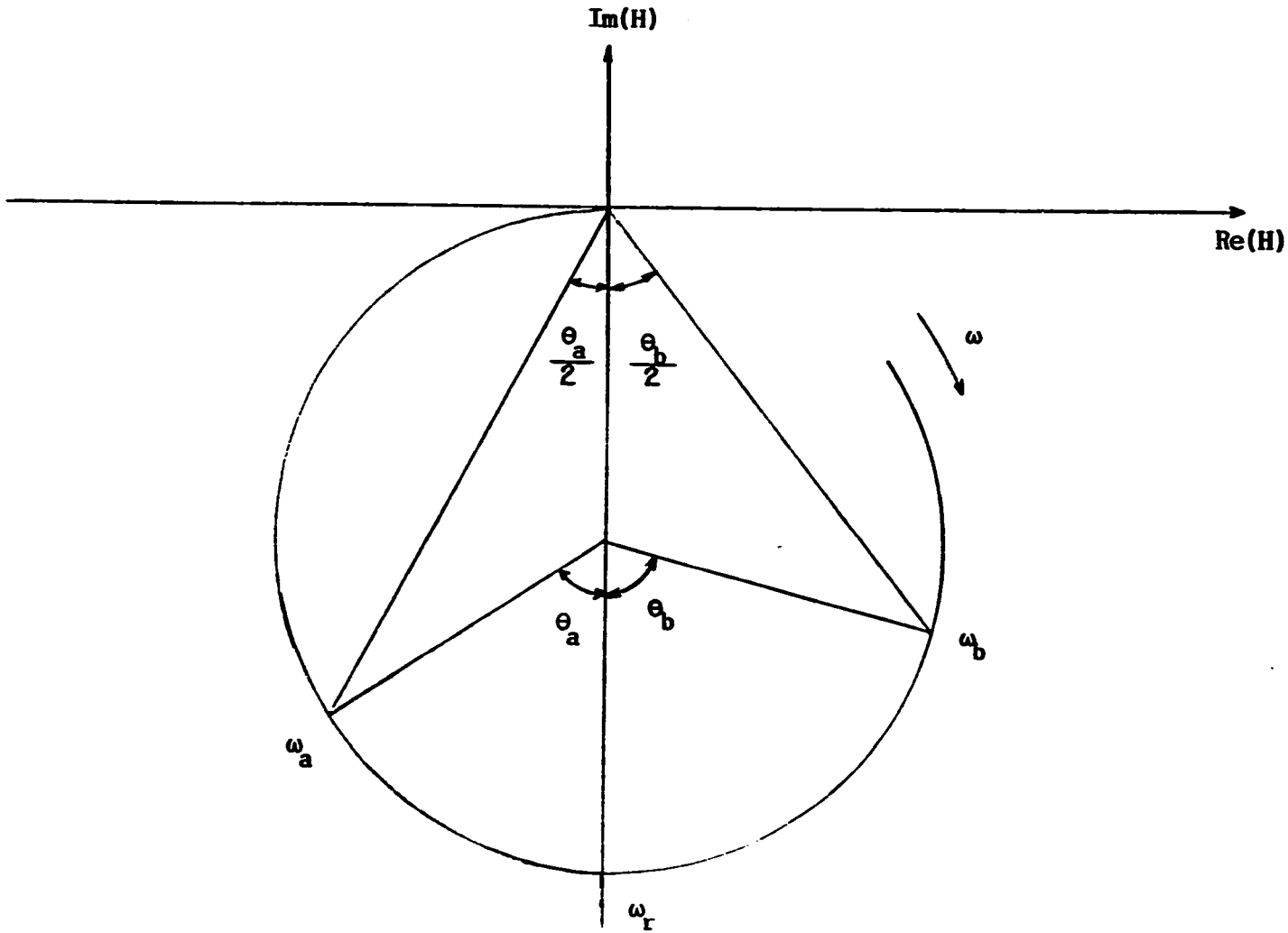

Fig. A.2. Details of Nyquist plot of FRF around natural frequency.

X. APPENDIX B. TRANSVERSE SENSITIVITY OF PIEZOELECTRIC ACCELEROMETER

The output voltage of an ideal piezoelectric accelerometer depends upon the direction of applied acceleration [21] and is given by

$$E_\theta = E_{max}\cos\theta \qquad \text{(B1)}$$

where E_{max} is the output in the direction of maximum sensitivity and θ is the angle between the direction of maximum sensitivity and the direction of acceleration. The directional dependence of sensitivity of an ideal accelerometer is shown in Fig. B1. If the maximum sensitivity is in the y-direction of Fig. B1, the sensitivity in the xy or yz plane is described by a figure-eight locus. It is the experimentalists efforts to minimize angle θ by aligning the direction of response and the direction of maximum sensitivity. The sensitivity at $\theta=90^o$ is called the transverse sensitivity. In an ideal accelerometer the transverse sensitivity is zero.

Because of practical manufacturing tolerances, the piezoelectric element in an accelerometer may not seat tightly against the frame, the mass may have an axial tilt, or the mounting stud or flat may vary slightly from the ideal direction. These factors create an effective angular tilt of the axis of maximum sensitivity. The effect of tilted axis of maximum sensitivity can be found by considering the orientation of the frame axes of accelerometer with respect to the piezoelectric

element axes. Instead of specifying nine direction cosines, the relationship between these two axes can be obtained by applying three successive rotations through Eulerian angles α, β, and γ as in Figure B2. The sequence of rotation is such that the first rotation through an angle α about axis X brings the triad into coincidence with axes x',y',z'. A further rotation β about axis y' puts the axes into orientation x'',y'',z''. Finally, a rotation γ about z'' makes the triad coincide with the frame axes x,y,z. With this coordinate axis, the relationship between the sensitivities of piezoelectric element and those of actual accelerometer is given as

$$\begin{Bmatrix} S_x \\ S_y \\ S_z \end{Bmatrix} = \begin{bmatrix} c\gamma & s\gamma & 0 \\ -s\gamma & c\gamma & 0 \\ 0 & 0 & 1 \end{bmatrix} \begin{bmatrix} c\beta & 0 & -s\beta \\ 0 & 1 & 0 \\ s\beta & 0 & c\beta \end{bmatrix} \begin{bmatrix} 1 & 0 & 0 \\ 0 & c\alpha & s\alpha \\ 0 & -s\alpha & c\alpha \end{bmatrix} \begin{Bmatrix} S_X \\ S_Y \\ S_Z \end{Bmatrix}$$

$$= \begin{bmatrix} c\beta c\gamma & c\alpha s\gamma + s\alpha s\beta c\gamma & s\alpha s\gamma - c\alpha s\beta c\gamma \\ -c\beta s\gamma & c\alpha c\gamma - s\alpha s\beta s\gamma & s\alpha c\gamma + c\alpha s\beta s\gamma \\ s\beta & -s\alpha c\beta & c\alpha c\beta \end{bmatrix} \begin{Bmatrix} S_X \\ S_Y \\ S_Z \end{Bmatrix} \qquad \text{(B2)}$$

where S_x, S_y, S_z are sensitivities of actual accelerometer

S_X, S_Y, S_Z are sensitivities of piezoelectric element

$c\alpha$, $c\beta$, $c\gamma$ are $\cos\alpha$, $\cos\beta$, $\cos\gamma$, respectively

$s\alpha$, $s\beta$, $s\gamma$ are $\sin\alpha$, $\sin\beta$, $\sin\gamma$, respectively.

For an ideal piezoelectric element, S_Y is maximum sensitivity and S_X, S_Z are zero, therefore practical sensitivities of an accelerometer can be expressed in terms of maximum sensitivity of a piezoelectric element as

follows;

$$S_x = (\cos\alpha \sin\gamma + \sin\alpha \sin\beta \cos\gamma) S_{max}$$
$$S_y = (\cos\alpha \cos\gamma - \sin\alpha \sin\beta \sin\gamma) S_{max} \qquad (B3)$$
$$S_z = (-\sin\alpha \cos\beta) S_{max}$$

The directional dependence of an accelerometers' sensitivities are easily recognized.

Consider special case where angle $\alpha=0$ in Fig. B2, each accelerometer sensitivity can be redefined as

$$S_t = \sin\gamma S_{max}$$
$$S_p = \cos\gamma S_{max} \qquad (B4)$$
$$S_z = 0$$

where S_p is primary axis sensitivity, and S_t is transverse sensitivity. The maximum transverse sensitivity is defined as the percentage ratio of the transverse sensitivity to the primary axis sensitivity and is given by

$$\text{Maximum Transverse Sensitivity} = \tan\gamma \text{ X } 100\ \% \qquad (B5)$$

which is often provided as the specification for an accelerometer from the manufacturer [22]. For this special case, if the response to be measured is inclined by angle ϕ in the transverse plane (xz plane),

then more a general expression for the transverse sensitivity is given as

$$\% \text{ Transverse Sensitivity} = \tan\gamma \cos\phi \times 100 \qquad \text{(B6)}$$

from which familiar typical transverse sensitivity plot is drawn as in Fig. B3.

The problem in using Eq. (B6) is that it is impractical to specify angles γ and ϕ for a given accelerometer. Furthermore, the cross-axis plane of the accelerometer is no longer perpendicular to the maximum sensitivity axis which is tilted angle γ with respect to the primary sensing axis of the accelerometer. Therefore, Eq. (B6) is valid only when the motion is restricted in the cross-axis plane.

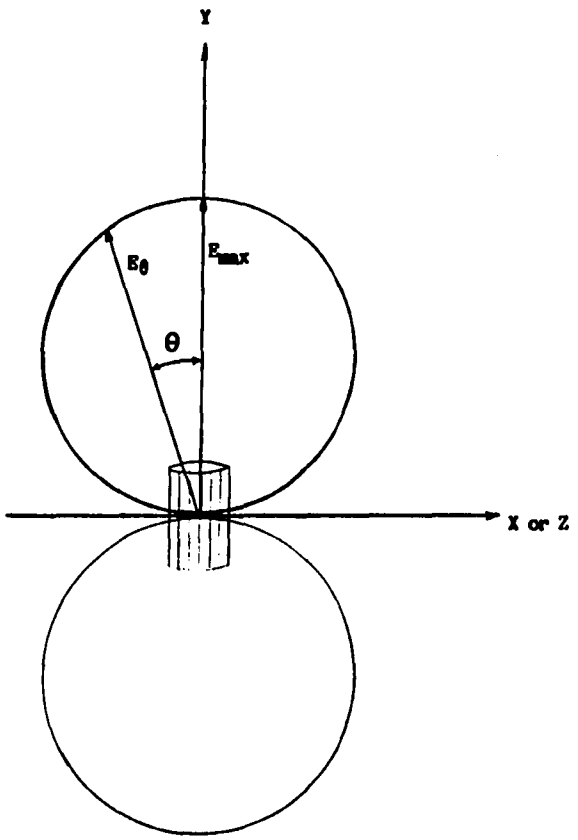

Fig. B.1. Directional sensitivity of an ideal seismic piezoelectric accelerometer.

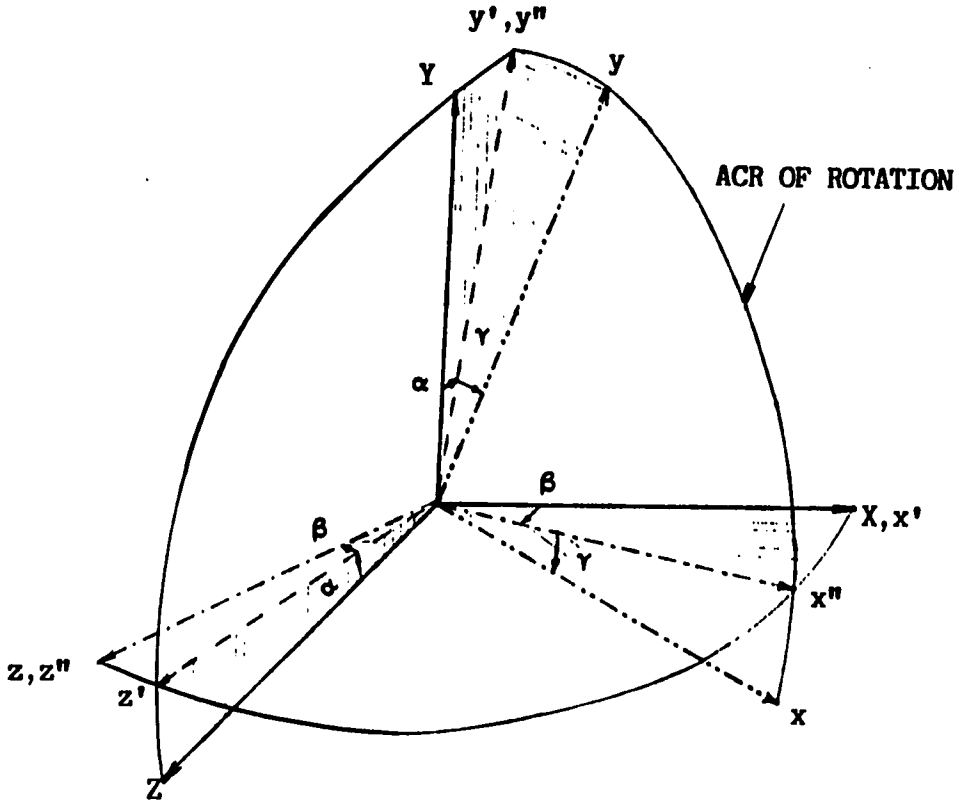

Fig. B.2. Orientation of tilted frame axes of accelerometer with respect to the piezoelectric element axes.
—— X Y Z : Original piezoelectric element axes.
---- x'y'z': First intermediate axes rotated angle α about X-axis.
— · — x"y"z": Second intermediate axes rotated angle β about y'-axis.
— · · — x y z : Final frame axes rotated angle γ about z"-axis.

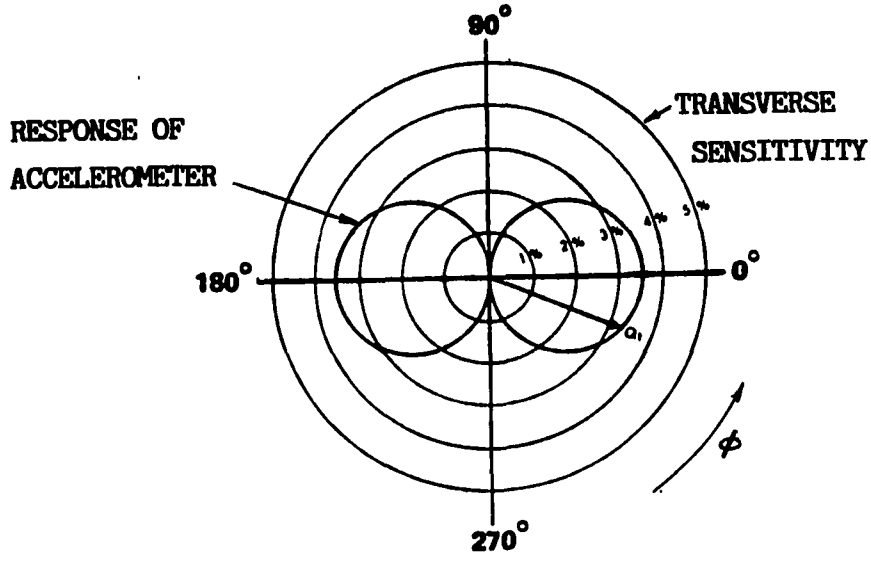

Fig. B.3. Typical transverse sensitivity plot for a piezoelectric accelerometer.